

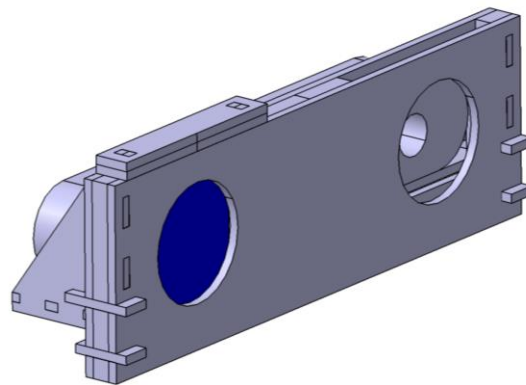
Semesterarbeit

Experimental Study on the Effects of Particle Impacts for Depth Measurements During Close-Range Proximity Flights

RT-SA 2017/3

Author:

Skuppin, Nikolai



Betreuer:

Dipl. Ing. Martin Dziura
Lehrstuhl für Raumfahrttechnik / Institute of Astronautics
Technische Universität München

Acknowledgments

Special thanks go to Dipl. Ing. Christian Bühler, who provided me with the samples and aided with challenges, such as the secondary damages on the Makrolon® samples. Furthermore, I thank Dipl. Ing. Martin Dziura for his confidence, the freedom in planning the experiments and for manufacturing the parts of the mount. I thank Flavio Rehn, who helped me to control the RACOON laboratory and to conduct the experiments.

Finally, I thank Denise Birk for her help and support during this challenging time.

Zusammenfassung

Die gegenwärtige Arbeit untersuchte den Einfluss von Partikeleinschlägen auf Optiken bei Nahbereichsoperationen zweier Raumfahrzeuge. Das Ziel war es, den allgemeinen Einfluss solcher Beschädigungen auf Stereovision-Systeme zu untersuchen. Des Weiteren sollte ein möglicher Zusammenhang zwischen Einschlagwinkel und zugehöriger Reduktion der Transmission auf die Qualität der Tiefenmessung untersucht werden. Hierzu wurde eine experimentelle Studie mit optischen Proben durchgeführt. Diese wurden durch Herrn Christian Bühler bereitgestellt und untersuchten Einschläge mit Modstaubsimulat. Die Untersuchungen fanden in einer repräsentativen Umgebung statt, welche durch das Robotic Actuation and On-Orbit Navigation Laboratory (RACoon) des Lehrstuhls für Raumfahrttechnik and der Technischen Universität München bereitgestellt wurde. Das Labor simuliert Nahbereichsoperationen mit Hilfe eines drehbaren Modells eines Zielsatelliten (Target) und einer beweglichen Sensorplattform, welche einen anfliegenden Satelliten simuliert (Chaser). Die Untersuchungen wurden mit einer auf diesem Chaser montierten ZED Stereokamera durchgeführt. Beschädigte und intakte Proben wurden vor den Linsen der Kamera platziert. Eine spezielle Halterung stellte die vergleichbare Positionierung sicher. Wichtige Kamera Einstellungen, wie zum Beispiel die Belichtungszeit wurden konstant gehalten um Vergleichbarkeit zwischen den Aufnahmen zu gewährleisten. Die Qualität der gewonnenen Tiefenbilder wurde anhand der Genauigkeit, Präzision und der Dichte der Tiefenbilder bewertet. Hierbei wurden Aufnahmen verschiedener beschädigter Proben mit einer gemeinsamen Referenzaufnahme verglichen. Die Genauigkeit wurde als mittlere Abweichung zwischen beschädigter und intakter Aufnahme definiert. Als dimensionslose Vergleichsgröße wurde eine relative Genauigkeit eingeführt, welche die Genauigkeit zweier Aufnahmen in Relation zur Präzision der Referenzmessung setzt.

Die Versuche bestätigten den negativen Einfluss der beschädigten Proben auf die Tiefenmessung. Für die relative Genauigkeit ergaben sich Werte zwischen 3.5 und 6. Jedoch ergaben sich für eine Kontrolle mit einer wiederholten Referenzmessung am Ende der jeweiligen Versuchsreihen Werte zwischen 1.5 und 3. Dieser ausgeprägte Messfehler verhinderte es einen Zusammenhang zwischen Einschlagwinkel und Genauigkeit der Tiefenmessung zeigen zu. Die Experimente brachten ähnliche Ergebnisse für die beiden untersuchten Materialien, Glas und Makrolon®. Jedoch wiesen die Makrolon® Proben sekundäre Beschädigungen auf. Diese ergaben relative Genauigkeiten von bis zu 12, was dem doppelten Wert der primären Beschädigungen entspricht.

Die Aussagekraft der Ergebnisse wird durch die Einschlaggeschwindigkeiten eingeschränkt, die mit 360 m/s weit unter den real erwartbaren liegen. Zudem wurden die Proben statt mit einzelnen Partikeln mit mehreren gleichzeitig beschossen. Neben der Reduktion des Messfehlers sollten sich zukünftige Versuche daher auf das Nutzen repräsentativer Proben konzentrieren.

Abstract

The present work investigated the influence of particle collision on optics during close range proximity operations of spacecraft. The purpose of the study was to examine the general impact of damaged optics on stereo vision between two spacecraft and to possibly link incidence angle and resulting reduction in transmission with the quality of the depth perception. Therefore, an experimental study with impacted optical samples was conducted. The samples were provided by Mr. Christian Bühler, who investigated impacts with lunar simulant. A representative environment was provided by the Robotic Actuation and On-Orbit Navigation Laboratory (RACOON-Lab) of the chair of astronautics at the Technical University of Munich. The laboratory simulates proximity operations with a rotatable target satellite mockup and a movable chaser sensor platform. The study used the ZED stereo vision camera, mounted to the chaser. Damaged and intact optical samples were placed in front of the camera lenses. A specially designed mount ensured proper placement. The camera settings, such as exposure, were kept constant, to ensure comparability. The quality of the resulting depth images was assessed by means of accuracy, precision and density of the depth maps. The trials with different damaged samples were all compared to a common reference measurement. The accuracy was defined as the deviation between impacted and reference measurement. Furthermore, a dimensionless relative accuracy, setting the accuracy in relation to the reference precision was introduced.

It could be shown that the damaged optics had the expected negative effect on depth perception. The relative accuracy was found to be in between 3.5 and 6. However, the relative accuracy for control measurements with intact samples at the end of the experiments produced values ranging from 1.5 to 3. This distinct error of measurement prevented the correlation between the impact angle and the depth accuracy. The experiments produced comparable results for the two investigated materials, silica glass and Makrolon®. However, the Makrolon® samples showed secondary damages. Measuring these secondary damages resulted in relative accuracies of up to 12, which represent twice the value of the primary defects.

The significance of the experiments was impaired by the impact velocities, which with a value of 360 m/s are far below the expected ones. Furthermore, the samples were impacted with multiple particles instead of single ones. Future experiments should, therefore, focus minimizing the error of measurement and using representative samples.

Table of Contents

| | | |
|----------|--|-----------|
| 1 | INTRODUCTION | 1 |
| 1.1 | Motivation | 1 |
| 1.1.1 | Space Environment | 2 |
| 1.2 | State of Technology | 2 |
| 1.2.1 | Depth Perception in Space Applications | 2 |
| 1.3 | Target | 3 |
| 1.4 | Methodology | 3 |
| 2 | TEST PLANNING | 4 |
| 2.1 | Requirements & Target | 4 |
| 2.1.1 | Sample Mount | 4 |
| 2.1.2 | Camera Script | 5 |
| 2.2 | Experimental Setup | 7 |
| 3 | PRINCIPLE OF STEREO VISION & METRIC | 9 |
| 3.1 | Stereo Vision | 9 |
| 3.2 | Post-Processing of Image Series | 11 |
| 3.3 | Accuracy and Precision | 11 |
| 3.3.1 | Relative Accuracy | 12 |
| 3.4 | Depth Density | 13 |
| 3.4.1 | Categorized Depth Density | 13 |
| 3.5 | Analysis Script | 14 |
| 4 | EXPERIMENTS | 16 |
| 4.1 | Feasibility Study | 16 |
| 4.2 | Universal Test Parameters | 17 |
| 4.3 | Study on Adequate Number of Images | 18 |
| 4.4 | Influence of Distance to Target | 19 |
| 4.4.1 | Glass | 19 |
| 4.4.2 | Makrolon® | 26 |
| 4.4.3 | Robustness of the Chaser Position | 28 |
| 4.4.4 | Conclusion | 29 |
| 4.5 | Fixed Distance from Target | 29 |
| 4.5.1 | Glass | 30 |
| 4.5.2 | Makrolon® | 32 |



| | | |
|------------|------------------------------------|-----------|
| 5 | DISCUSSION | 37 |
| 5.1 | Experiments | 37 |
| 5.2 | Application of Scenario | 40 |
| 6 | CONCLUSION | 41 |
| 7 | REFERENCES | 42 |
| A | APPENDIX | 44 |
| A.1 | Production Drawings | 44 |
| A.2 | Categorized Depth Densities | 47 |

List of Figures

| | | |
|------------|--|----|
| FIG. 2–1: | EXPLOSION VIEW OF THE SAMPLE MOUNT. | 5 |
| FIG. 2–2: | FLOW CHART OF THE CAMERA SCRIPT. | 6 |
| FIG. 2–3: | RACoon-LAB WITH ILLUMINATED TARGET SATELLITE, CHASER PLATFORM AND INSTALLED SAMPLE MOUNT. | 8 |
| FIG. 3–1: | PRINCIPLE OF STEREO VISION. OBJECTS BEING FURTHER AWAY FROM THE CAMERA APPEAR CLOSER TOGETHER IN THE IMAGES, WHEREAS CLOSER OBJECTS ARE MORE SEPARATED. | 10 |
| FIG. 3–2: | FLOW CHART OF THE ANALYSIS SCRIPT. | 15 |
| FIG. 4–1: | UNDISTURBED IMAGE OF THE LEFT CAMERA. | 16 |
| FIG. 4–2: | IMAGE OF THE RIGHT CAMERA, WITH IMPACTED SAMPLE IN FRONT OF THE LENS. | 16 |
| FIG. 4–3: | DEPTH IMAGE. THE RESULTING DEPTH IMAGE AS A GREYSCALE IMAGE. | 16 |
| FIG. 4–4: | CONFIDENCE IMAGE. THE RESULTING CONFIDENCE IMAGE AS A GREYSCALE IMAGE. | 16 |
| FIG. 4–5: | EVOLUTION OF PRECISION AND ACCURACY OVER NUMBER OF IMAGES. | 18 |
| FIG. 4–6: | REFERENCE IMAGE IN EXPERIMENT POSITION 1. | 21 |
| FIG. 4–7: | REFERENCE IMAGE IN EXPERIMENT POSITION 2. | 21 |
| FIG. 4–8: | RELATIVE ACCURACY FOR GLASS WITH VARIABLE TARGET DISTANCE. | 23 |
| FIG. 4–9: | CATEGORIZED DEPTH DENSITIES FOR GLASS WITH VARIABLE TARGET DISTANCE. THE POINTS MARKED IN RED ARE FROM EXPERIMENT POSITION 1 AND THE BLUE ONES FROM POSITION 2. | 25 |
| FIG. 4–10: | IMAGE OF THE LEFT CAMERA WITH LIMITED FIELD OF VIEW IN POSITION 1. | 27 |
| FIG. 4–11: | IMAGE OF THE LEFT CAMERA WITH LIMITED FIELD OF VIEW IN POSITION 2. | 27 |
| FIG. 4–12: | RELATIVE ACCURACY FOR MAKROLON® WITH VARIABLE TARGET DISTANCE. | 28 |
| FIG. 4–13: | IMAGE OF THE EXPERIMENTAL SETUP. THE BLACK CARDBOARD COVERS PREVENT THE INCIDENCE OF LIGHT. THE CLAMPS HOLD THE SAMPLES IN POSITION. | 30 |
| FIG. 4–14: | IMAGE OF THE LEFT CAMERA FOR TRIAL GREF. | 31 |
| FIG. 4–15: | IMAGE OF THE LEFT CAMERA FOR TRIAL G15. | 31 |
| FIG. 4–16: | RELATIVE ACCURACY FOR GLASS WITH FIXED TARGET DISTANCE. | 32 |
| FIG. 4–17: | IMAGE OF THE LEFT CAMERA FOR TRIAL MREF. | 34 |
| FIG. 4–18: | IMAGE OF THE LEFT CAMERA FOR TRIAL M75. | 34 |
| FIG. 4–19: | IMAGE OF THE LEFT CAMERA FOR TRIAL M0. | 34 |
| FIG. 4–20: | IMAGE OF THE LEFT CAMERA FOR TRIAL M03MM. | 34 |
| FIG. 4–21: | RELATIVE ACCURACY FOR MAKROLON® WITH FIXED TARGET DISTANCE. | 36 |
| FIG. 6–1: | CATEGORIZED DEPTH DENSITIES FOR MAKROLON® WITH VARIABLE TARGET DISTANCE. THE POINTS MARKED IN RED ARE FROM EXPERIMENT POSITION 1 AND THE BLUE ONES FROM POSITION 2. | 47 |
| FIG. 6–2: | CATEGORIZED DEPTH DENSITIES FOR GLASS WITH FIXED TARGET DISTANCE. THE RED AND BLUE POINTS ARE FROM TWO CONSECUTIVE IMAGE SERIES. | 48 |
| FIG. 6–3: | CATEGORIZED DEPTH DENSITIES FOR MAKROLON® WITH FIXED TARGET DISTANCE. THE RED AND BLUE POINTS ARE FROM TWO CONSECUTIVE IMAGE SERIES. | 49 |



List of Tables

| | |
|--|----|
| TABLE 4-1: AXIS SETTINGS OF RACOON LAB. THE CHASER AND TARGET POSITION ARE GIVEN IN STEPS FOR RACOON LABORATORY COMMAND INTERFACE. | 17 |
| TABLE 4-2: CAMERA SETTINGS PROVIDED BY AUTOMATIC MODE. THE SETTINGS FOR CAMERA PARAMETERS, WHICH WERE USED FOR THE SUBSEQUENT EXPERIMENTS..... | 19 |
| TABLE 4-3: SAMPLE ORIENTATION VARIABLE GLASS. ORIENTATION IS BOTTOM (B), TOP (T), LEFT (L), RIGHT (R). | 20 |
| TABLE 4-4: PRECISION AND ACCURACY OF VARIABLE GLASS EXPERIMENT..... | 22 |
| TABLE 4-5: SAMPLE ORIENTATION VARIABLE MAKROLON®. ORIENTATION IS BOTTOM (B), TOP (T), LEFT (L), RIGHT (R)..... | 26 |
| TABLE 4-6: PRECISION AND ACCURACY OF VARIABLE MAKROLON® EXPERIMENT. | 27 |
| TABLE 4-7: DEVIATION OF CHASER POSITION RESULTING FROM MOVING THE PLATFORM..... | 29 |
| TABLE 4-8: SAMPLE ORIENTATION FIXED GLASS. ORIENTATION IS BOTTOM (B), TOP (T), LEFT (L), RIGHT (R). | 30 |
| TABLE 4-9: PRECISION AND ACCURACY OF FIXED GLASS EXPERIMENT. | 32 |
| TABLE 4-10: SAMPLE ORIENTATION FIXED MAKROLON®. ORIENTATION IS BOTTOM (B), TOP (T), LEFT (L), RIGHT (R). | 33 |
| TABLE 4-11: PRECISION AND ACCURACY OF FIXED MAKROLON® EXPERIMENT | 35 |

Symbols

| | | | |
|-----------|----------------------------------|----------|---|
| N | number of images | I_{xy} | number of measurements with valid depth information at pixel x, y |
| Z_{max} | maximum depth | b | baseline |
| Z_{min} | minimum depth | z | depth |
| Z_{xy} | depth value of pixel x, y | f | focal length |
| C_{xy} | confidence value of pixel x, y | d | disparity |
| C_{lim} | confidence threshold | | |

Abbreviations

| | | | |
|--------|---|---------|---|
| API | Application Programming Interface | SDK | Software Development Kit |
| ESA | European Space Agency | SPHERES | Synchronized Position Hold, Engage, Reorient, Experimental Satellites |
| Fig. | Figure | TOF | Time of Flight |
| ISS | International Space Station | TUM | Technical University of Munich |
| LRT | Lehrstuhl für Raumfahrttechnik | VERTIGO | Visual Estimation for Relative Tracking and Inspection of Generic Objects |
| RACOON | Robotic Actuation and On-Orbit Navigation | | |

1 Introduction

1.1 Motivation

The increasing risk for space missions' due to space debris and uncontrolled objects leads to the awareness for the need of servicing and deorbit missions for spacecraft. The number of catalogued debris objects has constantly risen over the past years. There are also single events leading to a drastic increase of debris. Such an incident is a Chinese antisatellite test in 2007 [1], where the Fengyun-1 satellite was hit by a missile. Due to the orbital constellation, the produced debris cloud is long-lived and imposes a risk on other spacecraft. The constant monitoring and orbit prediction of detectable debris parts regularly leads to evasive maneuvers of satellites and spacecraft, including the international space station (ISS). Additionally, abandoned spacecraft pose a risk to other spacecraft, directly through collision, or indirectly through collision with space debris and resulting fragmentation. The consequences could be a self-energizing process, where the number of space debris rises uncontrolled, known as the "Kessler Syndrome"[2]. The awareness for the resulting risk to space missions has risen and several methods to reduce the amount of space debris are investigated [2]. An example would be a dedicated mission to deorbit an abandoned satellite. The necessary technology is currently being investigated. The SPHERES VERTIGO project on the ISS, for example, uses free-floating satellite mockups within the space station to develop and test navigation and feature detection software in zero gravity conditions [3].

Another facility concentrating on proximity operations between an uncooperative target and an approaching servicer is the Robotic Actuation and On-Orbit Navigation Laboratory (RACOON-Lab) of the institute for astronautics (LRT) at the Technical University of Munich (TUM). The facility consists of a pivot-mounted target satellite mockup and a movable chaser satellite, implemented as a sensor platform. The facility also hosts a spotlight simulating the sunlight. With the associated software interface, the laboratory allows for the realistic simulation of proximity operations between the two spacecraft. The sensor platform currently hosts a Microsoft Kinect v2 camera, and the ZED camera from Stereolabs. These two cameras are used to generate depth images of the target satellite and recreate its motion. They use different principles to generate the depth map. The Kinect uses the time of flight (TOF) method, where an infrared pattern is emitted by the camera, reflected by the object and recorded by the camera. By taking the time between emission and recording, the depth can be calculated. The ZED camera relies on the principle of stereo vision. Thereby, the camera takes two images of the same scene, from two different positions, which are separated by a baseline b . Like the human depth perception, these two images are compared and matched. With the given camera parameters, this displacement can be converted to a depth value. For a detailed description of this concept, please see chapter 3.1.

This study used the ZED camera and the RACOON laboratory to study the influence of dust impacts on the stereo vision performance in proximity operations of spacecraft. Thereby, the need for preventive measures can be assessed.

1.1.1 Space Environment

The environmental conditions, in which spacecraft operate are harsh. Therefore, material selection for spacecraft has to be performed with care [4]. Contamination of surfaces and impact of micrometeoroids and space debris are the main contributors for degradation of optics [4]. The latter can lead to a reduced transmission [4–6] and increased scatter [4], where the scatter leads to a decreased resolution and increased noise. Interplanetary dust particles and debris particles differ in their impact velocities. The first having averaged impact velocities of 20 km/s and the latter 10 km/s [7]. For debris particles in geostationary orbits this can become as low as some hundred meters per second [8]. These are only the averaged velocities and higher, as well as lower ones are possible. The defects resulting from impacts typically increase with particle size [7]. For 5-500 μm sized particles, the dust particles are expected to dominate the impact, while space debris dominates for the remaining sizes [4].

1.2 State of Technology

Stereo vision and 3D imaging has become a widespread and established technology. There are numerous possible applications, starting from industrial applications and collision avoidance in robotics [9] and ending with space applications on planetary rovers [10, 11]. With the Kinect camera from Microsoft, depth perception has also made its way to consumer electronics. There are several methods to extract depth measurements from a scene [9]. The focus of the present work is on stereo vision, which uses two images, taken with two cameras of the same scene.

1.2.1 Depth Perception in Space Applications

Stereo vision is a common technology on planetary rover missions. Stereo vision has been used on both the Mars Exploration Rovers [10] and the Mars Science Laboratory [11]. In this context, the influence of dusted optics has also been studied for the Mars Exploration Rovers [12]. There, the performance of stereo vision algorithms was tested, using a synthetic dust model. The model was found to produce realistic results, as it was compared to flight data from the rovers. In this case, flight data showed little influence of the dust contamination on the depth perception [12]. However, these results hold true for dust aggregating on the lens surfaces. The present work will focus on lens defects caused by dust impacts on the lens material.

Another application for depth perception concerns proximity operations between spacecraft. The ATV-5 mission, for example, tested a new laser-based docking sensor [13]. There are also experiments on the International Space Station (ISS) with the “Synchronized Position Hold, Engage, Reorient, Experimental Satellites” (SPHERES) [3]. These are carbon dioxide propelled model satellites, which are used inside the ISS to test navigation and proximity operations. The “Visual Estimation for Relative Tracking and Inspection of Generic Objects” (VERTIGO) experiment upgraded these satellites with a stereo camera for depth perception. There are recent experiments with self-supervised learning, using this infrastructure [14]. Thereby, the system learns to estimate the depth based on only one camera, in case the other camera breaks.

1.3 Target

The target of the present work is to study the effects of dust impacts on camera optics in proximity operations. Therefore, a study using the RACOON laboratory and its existing infrastructure was carried out. This facility belongs to the chair of astronautics at the Technical University of Munich (TUM). It allows the hardware in the loop simulation of proximity operations between a target satellite (target) and a servicer (chaser). The target is a scaled down mockup of a satellite with the ability of endless rotation in five axes. The chaser is a sensor platform with a total of six degrees of freedom. The walls of the facility are covered with black curtains to reduce reflection and hence background illumination. The facility also hosts an artificial sun with approximately 28% of the sun's intensity [15].

To ensure detailed documentation and to enable a scientific approach, a test scenario and an experimental setup were defined. One, or both available depth sensors, Kinect v2 and ZED were to be used. Furthermore, the institute's own accelerometer infrastructure could be used to generate specific samples. Of special concern was the repeatability of the experiments. It was not part of the present work to develop or compare different stereo vision algorithms and evaluate their handling of images from damaged optics.

1.4 Methodology

In a first step a test scenario was defined and the necessary infrastructure identified. The necessary and available optical samples were chosen and the experimental setup was arranged. This included the sample mount, to position the samples in front of the camera and a camera script, which allowed the display and saving of the respective images. This script was required, to ensure the images were all taken with equal settings, including parameters like brightness. These steps are described in more detail in chapter 2. Subsequently, the recorded depth images had to be post-processed and evaluated. First, a series of images was averaged over, to remove temporal noise, present in the images. Then, a variety of parameters of the images with defective samples were compared to an intact reference image. Chapter 3 addresses the basic principle behind stereo vision and describes the applied metric. Chapter 4 describes the single experiments and their evaluation. These include the preliminary ones, to demonstrate feasibility and define further experiment parameters, such as the number of images per series and the main experiments with the two types of material. The observed results are then discussed and set in context in chapter 5. The work closes with an outlook on possible follow-up experiments.

2 Test Planning

The aim was to study the effects of damaged optics on stereo vision in space applications. Yet, the velocities, required for interplanetary dust particles and fast-moving space debris, could not be produced with available particle accelerator. Therefore, the experiments were conducted with pre-existing samples. These samples, however, describe defects anticipated in lunar landing maneuvers [5, 6]. For these experiments 10 mg of moon simulant JSC-1A with sizes in between 250 and 350 μm were shot onto the probes with an approximate velocity of 360 m/s. The available materials were silica glass and polycarbonate (Makrolon®) [5, 6]. The first set of samples had a number of samples with a 0° (normal) impact angle [6]. The second set had the same experiment settings, with additional angular variation of the impacts [5]. The incidence angle of the particles was varied in 15 degrees steps from 0° (normal) to 75° from normal. Subsequent measurements of the transmissivity showed dependence on the incidence angle [5]. While these samples have a limited applicability for in orbit conditions, they are well characterized and therefore a good baseline. The experiments aim to identify a possible correlation between stereo vision performance and the impact incidence angle on the one hand and the correlated transmissivity on the other hand.

2.1 Requirements & Target

2.1.1 Sample Mount

As it is impractical to bring the lens defects directly onto the camera optics and the samples were already present, it was decided to build a sample mount for the camera where different probes could be tested without damaging the camera itself. The samples and the design of the camera imposed some requirements on the mount. The first one is to bring the sample close to the camera surface and to prevent incidence from background light, as this leads to reflections and image artifacts. The second is the possibility to adjust the probes in a controlled and defined way. This is necessary, as the impact sites are scattered around the center of the sample by up to 5 mm, due to natural scattering in the accelerator. The third one is to secure the samples from falling of the mount in case of an emergency shutdown of the laboratory.

As the second requirement proved to be the most important, the mount is designed to easily allow the adjustment of the sample. Therefore, a nominal position was defined, where the perfect centered defect is in the center of the camera lens. To allow the horizontal adjustment of the samples, a millimeter scale was added to the surface. This helps to log the position of the specimen holder. Polystyrene plates of 1 mm thickness were used for vertical correction of the impact site. Since the definition of the nominal position requested precise functional surfaces, it was decided to laser the parts from a hardboard panel. This manufacturing technique required the mount to be composed of several plates, but allowed fast prototyping of the mount and simple redesign. This is beneficial, as the Makrolon® samples are prone to scratches and had secondary defects from handling. A second front plate with reduced hole diameters was manufactured, which permitted to shroud the scratches.

Fig. 2–1 shows an explosion view of the mount. In the upper left corner is a placeholder of the camera, which is not part of the mount. The blue colored plate represents a

sample. The specimen holder itself is depicted in assembled configuration, but like the mount itself, is composed of four plates. The mount relies on the concept of form closure. Therefore, only some parts must be glued together, while the clear majority may be easily assembled and disassembled. The specimen holder is fixed to the mount by clamps, which are not depicted. All parts except of a placeholder plate between mount and camera were cut from 3 mm thick material. The middle part of the mount is formed by two identical plates and is in total 6 mm thick. During the experiments, cardboard covers between mount and camera were used to reduce the incidence of light from the background and resulting reflections within the mount. Additionally, for some samples a modified specimen holder was necessary. These samples were 50x60 mm in size and the length of the holder was increased by 10 mm. The mount itself is joined to the camera and the chaser platform by a screw. Dimensioned production drawings of the single parts can be found in 7A.1.

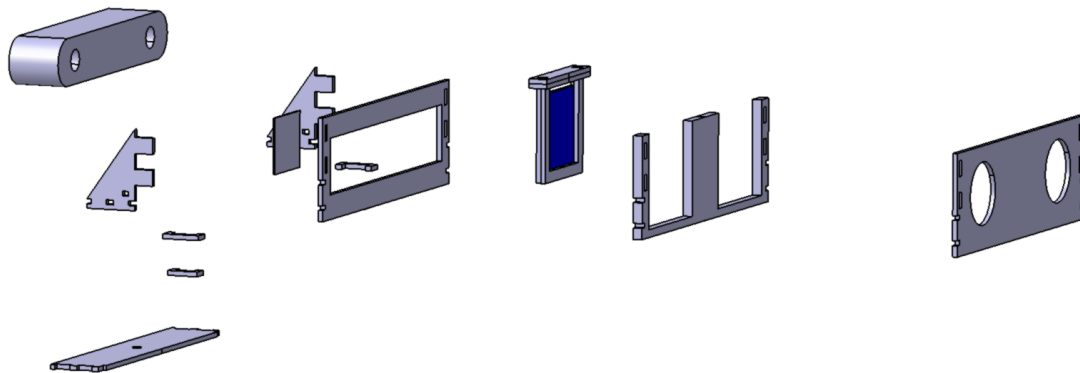


Fig. 2–1: Explosion view of the sample mount.

2.1.2 Camera Script

The performance of the camera is highly dependent on the surrounding conditions and the camera settings. While the surrounding environment is controlled through the laboratory, there was the need for a program to retrieve camera images with comparable settings. The ZED camera comes with an application-programming interface (API), which allows basic control over the camera settings and functions. The examples “SaveDepth” and “zed-opencv” were used as references for the developed program. These are distributed with the software development kit (SDK) and can be retrieved from the Stereolabs GitHub [16, 17].

The camera provides access to the unprocessed, as well as to the processed images. Additionally, the disparity map, the derived depth map and a corresponding confidence map can be obtained. The unit of the disparity is pixels. The depth unit can be freely chosen and is set to millimeters. The confidence is given as a value between 0 and

100, where the greater values represent less reliable measurements [18]. Fig. 2–2 shows the program flow of the camera script.

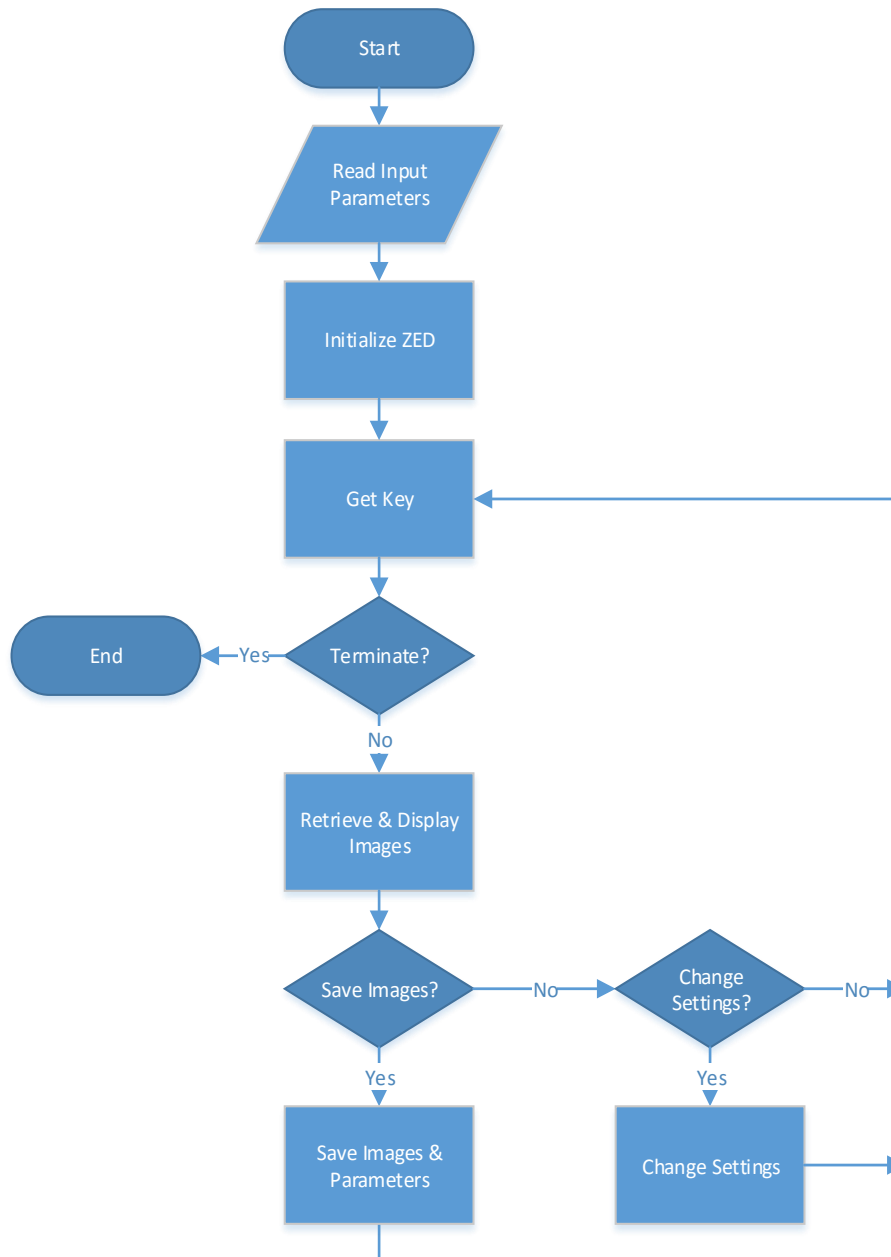


Fig. 2–2: Flow chart of the camera script.

The program consists of a starting sequence, where input parameters are loaded and the camera is initialized and a main loop, where images are retrieved, displayed and saved upon request. In addition to the images, camera parameters and settings are saved for later comparison. At the start, input parameters are read from a text file. Then, depending on the input, the camera is initialized with predefined settings, or in automatic mode, where the camera optimizes parameters on its own. Some settings are defined already in the program code and, therefore, inaccessible during runtime. The resolution is set to HD720 (1280*720 pixels), which is a tradeoff between the cameras maximum and the expected computational power onboard of a spacecraft. The depth mode, is set to “quality”, giving the best possible depth information [18].

Following the initialization, the program repeatedly retrieves and displays the provided depth, confidence and color image of the left camera. Different key events are defined and enable changing of settings during runtime. By pressing “+” or “-“, an internal counter is set to +1 or -1. Pressing keys “1” to “8” then alters the respective settings. These are in order of appearance: brightness, contrast, hue, saturation, gain, exposure, white balance and auto white balance. The new value for the respective setting is then displayed. Due to dependencies among the settings, some might be unchangeable, for example if exposure is set in automatic mode, the gain cannot be changed.

On pressing “s” on the keyboard, the program saves the images of a predefined number of frames in a specified folder. Thereby, the program saves the depth and corresponding confidence images, as well as the rectified color images from both cameras. These could be used for a comparison of different stereo matching algorithms. Additionally, the program saves the corresponding camera parameters and settings. This allows the later control of the settings, to ensure all the images are taken with equal settings. Pressing “p” increases an internal counter and allows the recording of a further set of images without overwriting the previous. Entering “q” terminates the program.

Unfortunately, the ZED camera gives only little control over the post processing of the images. There are two sensing modes, called “standard” and “fill”. The latter provides a complete depth map without occlusions. The “standard” mode preserves occlusions and uses less post processing [18]. To preserve the effects of the damaged optics the images in the experiments were taken in “standard” mode. Additionally, the calculation of the confidence value is not accessible and therefore not comprehensible. Hence, the available confidence limit was set to the maximum possible value of 100. This ensures that all available data from the camera is retrieved and saved. A filtering of the data set according to confidence is only done later in the evaluation process. For a detailed description of this filtering, see chapter 3. There is an ongoing development process for the camera and regularly new versions of the software development kit are published. The first version of this script was written with the SDK 1.2.0, which, for example, did not allow the setting of the white balance. This version was only used for the feasibility tests, described in section 4.1. The following experiments were conducted with the SDK version 2.0.0, which should have an improved depth quality in “standard” mode [19]. An updated version 2.0.1 was already published, bringing some bug-fixes. The affected functions, however, are not used within the script and appear to be uncorrelated to the depth perception. Therefore, and for consistency with the results all experiments were conducted with version 2.0.0.

2.2 Experimental Setup

The general principle of the conducted experiments is to compare depth measurements with impacted samples in front of one lens to common reference measurements. The samples can be understood as filters brought in front of the lenses. The reference measurement is performed with intact samples in front of the lenses, as even these will change the incidence of light onto the camera. The recorded images show temporal variation, which is why they are averaged over. A description of this process is found in section 3.1. For every experiment position, a reference measurement with intact samples is recorded. Then one sample is exchanged with a

defective sample and the measurement is repeated. The aim is to study the impact of the defects on the depth measurement and to possibly find a correlation between performance and impact angle of the particles. Therefore, parameters expected to have an influence on the performance are identified. To limit the number of experiments to a feasible amount, single parameters are selected for variation. These are, the type of material, the impact angle of the particles and the distance to the target. The first two are given by the available samples, while the latter has an influence on the depth error [20]. Furthermore, the distance changes the image section occupied by the target. At the same time the image section, affected by the impact, stays constant. Therefore, moving the camera to different distances from the target should have a noteworthy influence on the quality of the recorded depth images.

All measurements are performed in an artificial environment, provided by the RACOON laboratory, simulating the relevant orbital conditions. These are formed by the target satellite mockup, the dark background and the distinct lighting from the artificial sun. The experiment is designed to identify relative differences between the samples without quantifying the true performance. Therefore, environmental perturbations of the laboratory, not present in orbit should be averaged out. These are for example dust floating in the air or light reflection inside the laboratory. Fig. 2–3 shows the experiment setup with the target satellite and the chaser platform. On the top of the platform the ZED camera and the mount can be identified. Noticeable are the clamps, used to fasten the specimen holders to the mount. Black cardboard covers can be seen below the clamps. These were necessary to prevent background illumination of the samples and resulting reflection. The target satellite and the chaser platform are brightly illuminated by the artificial sun, which is approximately to the rear. Further description of the single experiments is found in chapter 4.

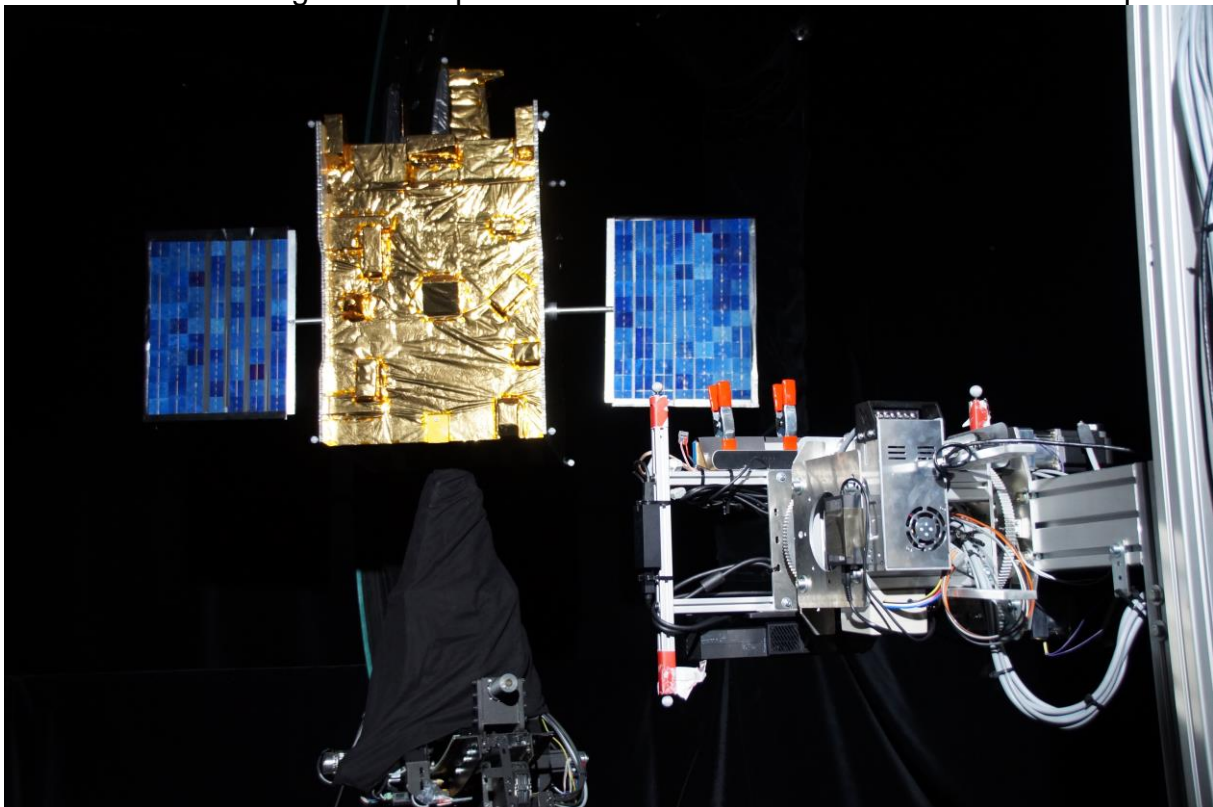


Fig. 2–3: RACOON-Lab with illuminated target satellite, chaser platform and installed sample mount.

3 Principle of Stereo Vision & Metric

Two types of parameters are used to assess the quality of the recorded depth maps. The is described in [21] and relies on the calculation of the accuracy and precision of the measurements in the nominal and in the defective case. As the ground truth, necessary for the calculation of the accuracy, is not available, it is substituted with the reference measurement. The accuracy therefore, can be interpreted as the ability to repeat the reference measurement. This approach allows the comparison of different defective samples, as they are compared to the same reference scene. The second parameter is the density of the depth map, as described in [12], giving general information on the depth perception. It is defined as the ratio of pixels with identified depth information to the total number of recorded pixels. The benefit of this metric is that it accounts for the occluded pixels, as these have no valid depth value assigned to.

Since the depth images show temporal variation, it would be insufficient to rely on only one measurement. Therefore, in every setup, a series of N images is taken and post-processed. The ZED camera provides depth, as well as confidence images. The former ones contain the depth information and the latter ones give further information on the reliability of the corresponding depth values. The depth image keeps the depth as a real number between the specified minimum and maximum distance. Pixels with no depth information, due to violation of the specified borders or occlusion in the image, are marked by a value of zero.

3.1 Stereo Vision

Stereo vision in general relies on two images of the same scene taken with two cameras separated by a baseline distance b . These two images are processed so that for each pixel in the first image the corresponding pixel in the second image is found. The distance between these two pixels in the universal image frame is called disparity d . Due to similarity between the parameters the following equation holds:

$$\frac{z}{b} = \frac{f}{d} \quad \text{Eq. (3-1)}$$

where b is the baseline, d is the disparity, f is the focal length and z is the depth. Therefore, it is possible to calculate the distance z for each pixel in the image, if the baseline and focal length are known [20].

To ease the matching of the images they are first post-processed. This is done to correct camera and alignment errors. First, misalignment is corrected and lens distortion compensated. In the next step, the images are rectified. Thereby, the images are transformed, so that they align for example horizontally. This means that two pixels showing the same feature in the two images are just separated horizontally and not vertically. Therefore, the complexity of matching the images is reduced, as for one given pixel p_{xy} in the first image, just pixels p_x with fixed y in the second image must be considered. To obtain the necessary transformation coefficients for alignment correction and rectification the stereo system must be calibrated. An established method is the usage of checkboard patterns with known edge length.

After this processing, the two images are compared to each other and the disparities are calculated. Assigning disparity values to single pixels in the images is the core

problem of stereo vision. There are numerous approaches to solve this problem [22] and there is constant improvement. The Middlebury Stereo Vision Page [23] regularly updates a list of stereo vision algorithms and their performance on defined test data sets. The detailed description of the different algorithms and methods is beyond the scope of this thesis. Yet, the general approach is to maximize the correspondence between pixels in the two images. The matching of images is especially difficult in texture-less areas, or if a feature is occluded in one of the images. For texture-less areas a pixel in one image can correlate with a multitude of pixels in the second image. For an occluded area, it is impossible to identify a matching pixel. There are, however, methods to remove occlusions from images by additional post-processing [18, 24]. Yet, these methods are prone to errors, as they try to produce information where it is already lost.

Fig. 3–1 illustrates the whole concept of stereo vision and the relation between disparity and depth. The blue object is further away from the camera and the corresponding pixels appear closer together. Furthermore, the corresponding pixels appear on the same line of the images. The view on the yellow object is blocked by the red one and hence only visible in the right image. This makes it impossible to find a matching pixel in the left image. Additionally, the homogeneous background offers no features for the matching, which makes assigning a depth value difficult.

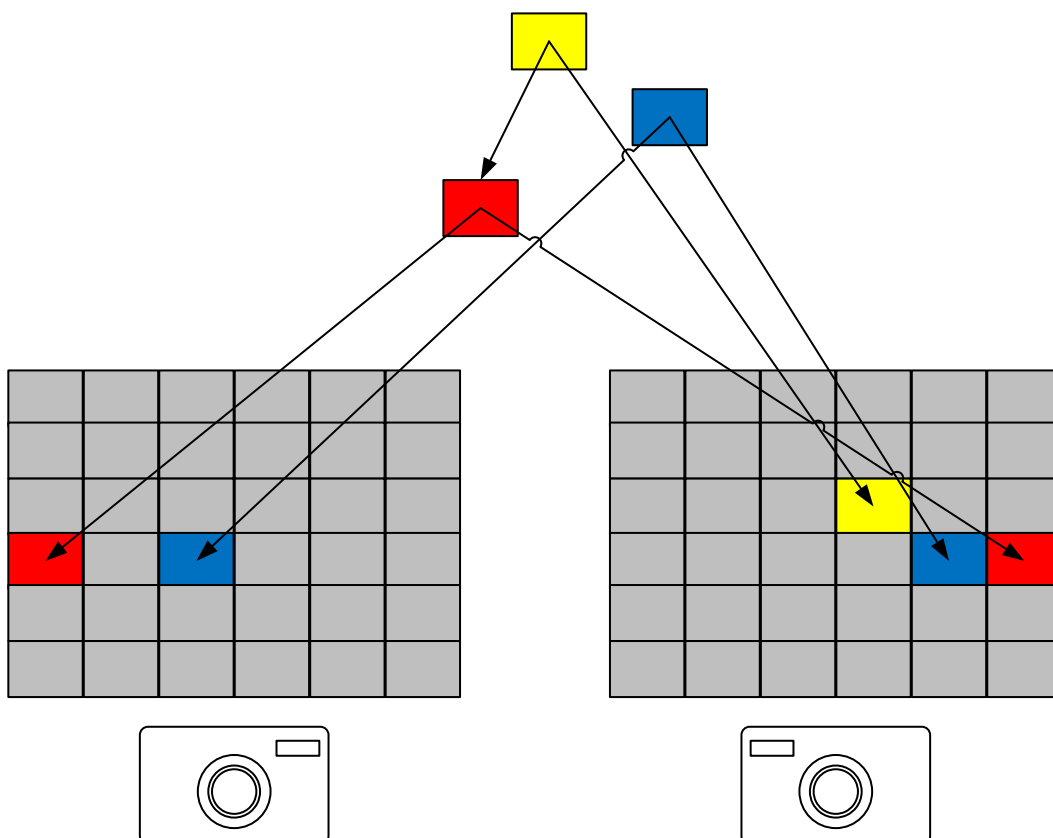


Fig. 3–1: Principle of stereo vision. Objects being further away from the camera appear closer together in the images, whereas closer objects are more separated.

A different method to generate depth images is based on the principle of time of flight (TOF). This method is, for example, used by Microsoft's Kinect v2 camera. An

emitter sends out infrared rays, which are reflected by the target and received by the camera. Taking the time between emission and recording, it is possible to calculate the distance of the target. The benefit of this active measurement method is that it works in low light to dark environments, as it is not dependent on a well illuminated scene.

3.2 Post-Processing of Image Series

Every image is initially filtered by depth, setting pixels with $Z_{max} < Z_{xy} < Z_{min}$ to zero. This step ensures that outliers are removed. In a further step, the depth image is filtered according to the confidence image provided by the camera, setting depth values z_{xy} with confidence levels $c_{xy} > c_{lim}$ to zero. The camera has identical filters implemented. However, to allow the adaption of the filter parameters in the later process, the images are recorded with minimal filtering. These N filtered images are then averaged. As the depth values of zero are arbitrary and present no real-world depth information, these values are excluded from the calculation of the average. The average depth for the pixel with coordinates x and y is, therefore, calculated as followed:

$$\bar{z}_{xy} = \frac{1}{I_{xy}} \sum_{n=1}^N z_{xy}^n \cdot \{z_{xy}^n \neq 0\} \quad \text{Eq. (3-2)}$$

where I_{xy} is the number of depth values unequal zero for the specific pixel x, y and z_{xy}^n the depth value in image n . Additionally, the ratio between zero measurements $N - I_{xy}$ and total measurements N is considered. If this is greater or equal to 0.5 the according measurements z_{xy} are marked as unreliable and set to zero. Therefore, the averaged depth value for the given pixel also becomes zero. This ensures that single erroneous measurements are excluded from further processing, as only pixels where more than half have a valid measurement are assigned a depth value. A related median filter for the temporal fusion of data is described in [25].

A second method is to mark pixels with a zero in one of the N images as unreliable and, therefore, assign a value of zero to the averaged pixel. This prevents possible oscillations, where pixels are in- or excluded depending on the number N of images considered. A further evaluation of the two described methods is found in section 4.3.1.1. This found the second method to be more stable, which is why it was used for the remaining experiments.

3.3 Accuracy and Precision

As described in [21] depth measurements can be characterized by the measurement accuracy and precision. The first quantity describes the deviation between the true depth value and the measurement, the second one the variation between single measurements. The accuracy can be calculated as followed [21]:

$$A = \frac{1}{XY} \sum_X \sum_Y |\bar{z}_{xy} - z_{xy}^*| \quad \text{Eq. (3-3)}$$

A is the accuracy, X and Y describe the resolution of the image, z_{xy} is the depth of pixel x, y , where $*$ denotes the ground truth and the overbar marks the averaged value over N measurements. The precision P is calculated as followed [21]:

$$P = \frac{1}{XY} \sum_X \sum_Y \sqrt{\frac{1}{N} \sum_N (z_{xy}^n - \bar{z}_{xy})^2} \quad \text{Eq. (3-4)}$$

The variables are equivalent to the aforementioned. X and Y describe the image resolution, N is the number of measurements and z_{xy} is the depth of pixel x, y in measurement n or averaged, respectively.

The above-mentioned formulas, however, are adapted for the usage with the recorded data. Due to the filtering, the depth maps are incomplete, so that only parts of the images contain real measured values, while others hold the arbitrary value of zero. It would be wrong to treat these values like the measured data, as it would lead to incorrect precisions. Additionally, there is no ground truth available, which makes the calculation of the accuracy in its original form impossible. Therefore, for the remainder of this work the term accuracy refers to the mean deviation between the measurements of the reference scene and the defective sample. Furthermore, the accuracy and precision were also considered on pixel level. This leads to the following formula, giving the accuracy per pixel A_{xy} . For the calculation of the average depth values see section 3.1. The asterisked value denotes the averaged measurement of the reference scene.

$$A_{xy} = |\bar{z}_{xy} - \bar{z}_{xy}^*| : \{\bar{z}_{xy} \neq 0 \wedge \bar{z}_{xy}^* \neq 0\} \quad \text{Eq. (3-5)}$$

The mean accuracy A is then calculated by averaging the accuracy per pixel with the number of pixels, where the accuracy is defined on. Please note that the accuracy is only defined for pixels where both averaged measurements are valid and, therefore, unequal zero. This is, because the zero value is arbitrary and would distort the accuracy. The precision on pixel level is given by the following formula, with I_{xy} being the number of measurements different from zero for this pixel. As with the accuracy this value is only defined for pixels, where the averaged measurement is valid and therefore unequal zero.

$$P_{xy} = \sqrt{\frac{1}{I_{xy}} \sum_{n=1}^N (z_{xy}^n - \bar{z}_{xy})^2 : \{z_{xy}^n \neq 0 \wedge \bar{z}_{xy} \neq 0\}} \quad \text{Eq. (3-6)}$$

The averaged precision P is calculated by taking the mean of all pixel precisions. With given accuracy and precision relative accuracy, described in the next section could be derived.

3.3.1 Relative Accuracy

The relative accuracy describes the deviation between the measurements and is calculated as followed:

$$D = \frac{A}{P^*} \quad \text{Eq. (3-7)}$$

where D is the metric value, A is the mean accuracy between reference and sample measurement and P^* is the average measurement precision of the reference scene. This parameter relates the observed difference between the measurements to the expected variation of the reference measurement. A value less or equal to one means

that the difference between the reference and the defective measurement is within the nominal measurement precision. The greater the parameter, the greater the negative impact of the defective sample.

The incomplete depth maps coming from the camera and the arbitrary definition of zero depth pixels make the calculation of accuracy and precision complex and biased. As it only allows the calculation of these parameters on a confined area, where valid depth measurements are available. The metrics neglect large areas of the images where there is no depth measurement at all or only in one of the two measurements, the reference or the defective sample. To take account of this information the depth density as described in section 3.4 was used.

3.4 Depth Density

The depth density is defined to be the ratio between the number of pixels with valid depth information, a depth different from zero, and the total number of pixels. This value is described in [12] as a metric for depth images.

3.4.1 Categorized Depth Density

The concept of depth density is extended to allow a detailed comparison between the measurements. Therefore, a comparative density between the averaged reference measurement and the averaged measurement was developed. Comparing these, five events can be identified. These are:

- No valid depth information in both measurements
- Valid depth information only for the defective measurement
- Valid depth information only for the reference measurement
- Valid depth information for both measurements, deviation less than averaged measurement precision of reference scene
- Valid depth information for both measurements, deviation greater than reference measurement precision

Each pixel of the averaged measurement is assigned to one of the categories. The number of pixels in each category is then divided by the total number of pixels, giving a density value for this category. As the categories are pairwise disjoint and complete, the sum over all categories is one. In addition, to comparing only both the averaged reference and disturbed images, every single disturbed image was compared to the averaged reference. Taking these values, it was possible to estimate the variance of the single densities.

This metric allows a differentiated comparison between several measurements as it accounts for the overall measurement and includes the measurement precision of the reference measurement. Considering the reference measurement as a baseline and assuming it to be the best possible, the metric allows good comparison on the impact of defects. However, this metric gives no information on the real quality of the measurement, being only a relative comparison to the baseline reference measurement, which is assumed to be the most reliable.

3.5 Analysis Script

The calculation of the metric parameters is implemented in MATLAB. This allows the sequential processing of the images. First, the reference images are loaded into the program. Each image is filtered according to confidence and depth. In addition, it is possible to apply a rectangular filter and remove perturbing areas, such as structures of the facility. Afterwards, all the already loaded images are averaged and the precision is calculated. This procedure is repeatedly done for one image up to N , the total number of images in one measurement. Thereby, it is possible to analyze the evolution of the precision over the number of images and the stability of the calculation process. After the reference images have all been loaded and processed, the program continues to the disturbed images. For each different sample the previous process is repeated and enhanced. Additionally, the accuracy in comparison to the reference sample and the relative accuracy, as well as the depth densities are calculated. As for the reference scene, the images are processed sequentially from one to the total number N , to illustrate the stability of the calculation. After all samples are processed, the program generates some graphs and tabulated output of the calculated parameters. Fig. 3–2 provides a flow chart of the analysis script.

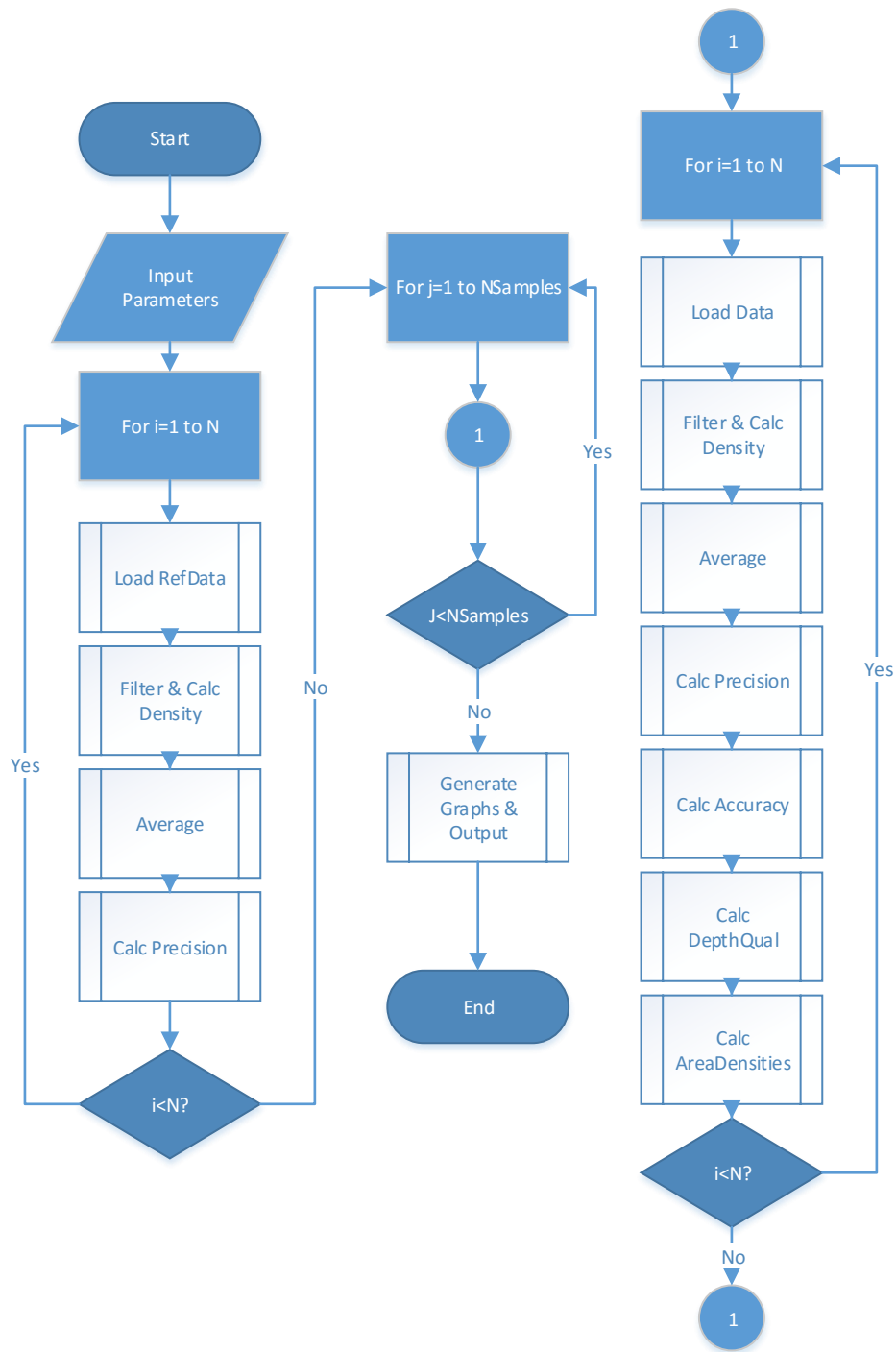


Fig. 3–2: Flow chart of the analysis script.

4 Experiments

The experiments can be subdivided into preliminary tests to ensure the camera is able to cope with the intact but also defective samples, and the main experiments, where the different samples were tested systematically.

4.1 Feasibility Study

The first test performed, aimed to ensure that the camera could process images with a defective sample in front of the lenses. Therefore, an impacted glass plate was placed in front of one lens.



Fig. 4–1: Undisturbed image of the left camera.

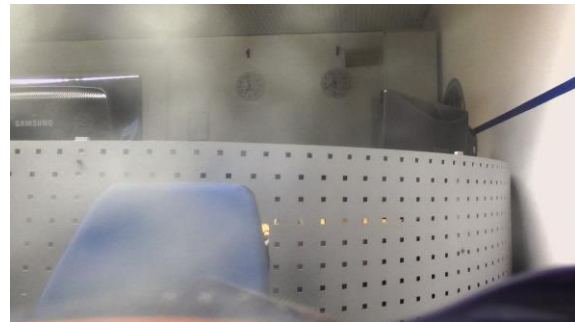


Fig. 4–2: Image of the right camera, with impacted sample in front of the lens.

Fig. 4–1 and Fig. 4–2 show color images taken with the camera. Fig. 4–2 shows the image taken with the right camera and a defective glass plate in front of the lens. The picture appears blurry, but most of the features are still identifiable. Additionally, there are some visible structures in the lower area and in the lower right corner. These show the improvised fixation of the plate.



Fig. 4–3: Depth image. The resulting depth image as a greyscale image.



Fig. 4–4: Confidence image. The resulting confidence image as a greyscale image.

Fig. 4–3 and Fig. 4–4 show the depth image and the confidence map of the scene. The confidence map in Fig. 4–4 shows clear similarity with the scene from figures Fig. 4–1 and Fig. 4–2. The depth map, however, has just basic commonality with the images.

These preliminary tests showed that depth images could be obtained with defective plates in front of the lens. However, it also showed the necessity of a mount, to hold the samples in a defined and precise position. Additionally, these tests were used to establish some requirements for the mount. The tests showed that, due to background

light, the samples reflected the surrounding room. Therefore, the samples should be brought as close to the lens as possible and incident background light should be reduced.

4.1.1.1 Evaluation

These experiments were not evaluated further. As they were just qualitatively in nature to demonstrate the feasibility of the set up and to develop the camera script. The tests showed that the camera could cope with the damaged optical samples and was able to generate depth images. Furthermore, these tests helped to derive requirements for the sample mount, as they showed the scattering of the defects and the problem of reflectivity of the samples.

4.2 Universal Test Parameters

All the remaining experiments were conducted in the RACOON lab with equal settings. There were two positions in different distances from the center of the target satellite. The first, called position 1 at approximately 3.5 m and position 2 at 2.0 m. The following Table 4–1 contains the target positions for the different axes of the RACOON laboratory. The units are given in steps, which is the native unit used by the laboratory control interface. The only difference between the two positions is the value of axis 0, which is the x translation of the chaser platform.

Table 4–1: Axis settings of RACOON Lab. The chaser and target position are given in steps for RACOON laboratory command interface.

| Axis | Position 1 | Position 2 |
|------|------------|------------|
| 0 | 59000 | 184500 |
| 1 | 31900 | 31900 |
| 2 | 0 | 0 |
| 3 | -135500 | -135500 |
| 4 | 0 | 0 |
| 5 | -77350 | -77350 |
| 6 | 0 | 0 |
| 7 | 0 | 0 |
| 8 | -6000 | -6000 |
| 9 | 0 | 0 |
| 10 | 30000 | 30000 |

All experiments were conducted with the artificial sun as the exclusive light source within the laboratory. Still a minimal background illumination from the laboratory was present. The orientation of the sun was selected to allow good illumination of the target,

without direct irradiation on the camera. Therefore, it was placed in the rear of the chaser to the left side at an approximate angle of 30°. This, however, allowed incidence of light on the chaser from behind. Since the preliminary tests showed the problem of reflection of the background by the samples (see section 4.1) a cardboard cover was used to shadow parts of the mount. This, however, did not cover the complete mount. Therefore, additional covers were introduced in some experiments. The position and orientation of the sun simulator could not be controlled at the time of the experiments. It was marked on the facility to allow the later extraction of the axis settings.

4.3 Study on Adequate Number of Images

This test was conducted in position 2 with a selected number of glass samples. For every sample, two datasets of the same scene and with the same configuration were recorded. This allowed not only the calculation of the measurement precision, but also the comparative calculation of the accuracy. Every dataset consisted of eleven images. The target was to identify a feasible number of images to allow stable values for accuracy and precision.

4.3.1.1 Evaluation

This experiment helped to assess, whether the taken number of eleven images was sufficient to enable a stable result and whether the recorded data were characteristic of the given scene.

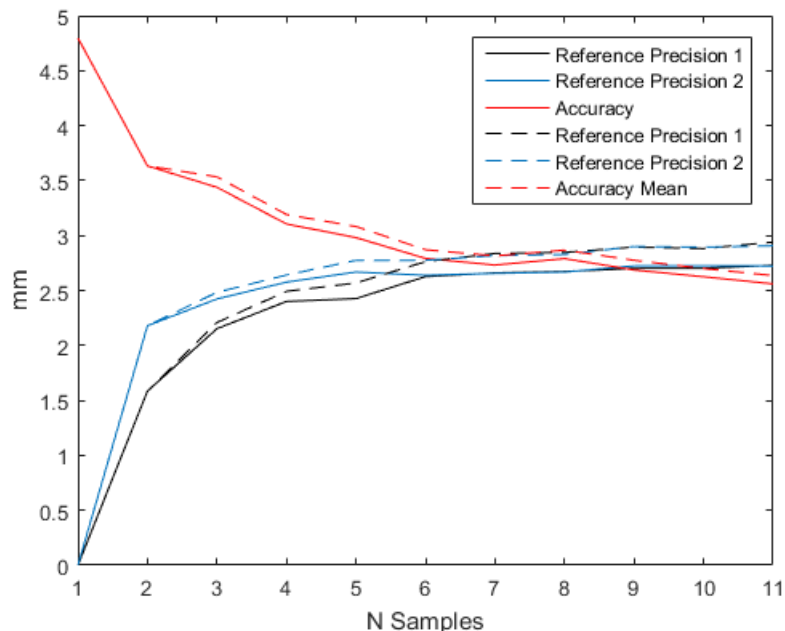


Fig. 4-5: Evolution of precision and accuracy over number of images.

Fig. 4-5 shows the evolution of the measurement precision and accuracy for one to eleven images. The x-axis shows the number of images considered for the calculation and the y-axis gives the precision and accuracy in millimeters. The two datasets were taken with intact glass plates in front of both cameras. The accuracy is the mean difference between the two datasets. The dashed and the solid lines represent different evaluation methods of the same dataset. The first one (dashed) averaged the non-zero

values of a pixel z_{xy} if more than half the pixels in N images were non-zero. Otherwise the averaged pixel was set to zero. The second method (solid) set the averaged pixel z_{xy} to zero if the corresponding pixel in at least one of the N measurements was zero, otherwise the pixels were averaged (see section 3.2). For the solid line the pixels of all measurements were considered. If in one of the N measurements one value for the specific pixel was zero, all according pixels were set to zero and, therefore, also the pixel in the averaged image. The precision of zero for only one image is due to the averaged measurement being equal to the measurement. The value then increases with increasing number of images and appears to approach an asymptotic solution. The same is true for the accuracy, even though its value is decreasing with increasing number of images. At seven to nine images the accuracy drops below the corresponding precision, which suggests that the difference between both measurements is within the measurement noise. In general, the solid lines are below the dashed ones. This indicates that the method provides better and more stable results. The observed trends were also visible for impacted samples.

The experiment on temporal stability showed that after approximately seven to nine consecutive measurements, the difference between two separate measurements of the same scene with unchanged conditions is within the measurement precision. Therefore, the selected number of eleven consecutive images appears to be sufficient to enable temporal stability and was chosen for the following experiments. Furthermore, it revealed the advantage of marking zero pixels as unreliable in the complete measurement. The benefit of this method is the stability. A pixel, once marked as unreliable due to a value of zero is completely removed from further evaluation. With the other method, it is possible for the pixel to be alternately considered and removed from the evaluation, leading to oscillation. For these reasons, the method setting all unreliable pixels to zero was used for analysis.

4.4 Influence of Distance to Target

4.4.1 Glass

The test procedure for the glass samples was as followed: First, the ZED camera was cleaned with a microfiber cloth used for cleaning of cameras. Afterwards the sample mount was installed on the chaser platform and the intact reference glass samples were inserted. Then the facility was powered up, target and chaser were brought position 1 and the artificial sun was lit. After approximately five minutes, the camera script was started in auto mode, where the camera can optimize the settings to the given situation. Two series of images were taken and the camera script was stopped. The saved output files provided the settings chosen by the camera. These were then set in the input file of the camera script for the subsequent experiments and can be found in Table 4–2.

Table 4–2: Camera settings provided by automatic mode. The settings for camera parameters, which were used for the subsequent experiments.

| Brightness | Contrast | Hue | Saturation | Gain | Exposure | White Balance |
|------------|----------|-----|------------|------|----------|---------------|
| 4 | 4 | 0 | 4 | 98 | 54 | 4600 |

With the defined settings, the camera script was started again in the experiment mode, where the settings are taken from the input file. After waiting for some seconds to avoid startup effects of the camera, a series on 11 images was taken. Then, the chaser was moved to position 2 and another set of 11 images was taken. Afterwards the camera script was stopped and the chaser returned to position 1. Subsequently, the chaser was lowered to allow the exchange of samples. Therefore, the position of axis three was set to a value of zero. Then, the first impacted sample was inserted into the mount. For the present experiments, the sample in front of the left camera was exchanged. The samples were placed so that the damaged side of the sample was opposed to the camera, as it is expected for impacts. The specimen holder was oriented, so that the damaged surface of the sample was protected from contact with the mount. This was to ensure that adhesive particles resulting from the impact experiments would stay in position and to prevent further scratching of the samples.

As described in section 2.1.1 the damage sites were scattered around the center, therefore, the defects were centered manually in front of the lens. Table 4–3 contains the trial name, sample number, orientation of the sample within the mount and the horizontal and vertical displacement of the mount. The orientation describes how the sample was inserted into the mount. All probes are marked with a number in one of the corners, giving the sample number. The orientation gives the position of this number as seen from the camera. This can be either top (T) or bottom (B) and left (L) or right (R). For the first two reference measurements, there is no orientation given, as orientation of the intact samples should have no influence on the results. The previously described procedure was repeated for every trial.

Table 4–3: Sample orientation variable glass. Orientation is bottom (B), top (T), left (L), right (R).

| Trial | Sample Number | Orientation | Horizontal displacement [mm] | Vertical displacement [mm] |
|-------------|---------------|-------------|------------------------------|----------------------------|
| GRefAutoSet | GRef | - | 0 | 0 |
| GRef | GRef | - | 0 | 0 |
| G0 | 0G | BL | 0 | 0 |
| G01mm | 0G | BL | 1 | 0 |
| G15 | 6 | TR | 6 | 3 |
| G30 | 7 | TL | 2 | 2 |
| G45 | 8 | TL | 3 | 0 |
| G60 | 9 | TL | 0 | 0 |
| G60Covered | 9 | TL | 0 | 0 |
| G75 | 10 | BR | 0 | 0 |
| GRef_End | GRef | BR | 0 | 0 |
| G0_end | 0G | BL | 0 | 0 |

Since the defects were centered manually in front of the camera, the influence of this process should be evaluated. Therefore, there are two measurements of sample 0G, which are displaced by 1 mm in the horizontal level. For sample 6, there was a visible incidence of light from the upper side of the mount. Sample 8 had an offset within the mount of approximately 0.5 mm vertically. This was due to the slight scattering in the sample size, which prevented the nominal positioning. For samples 9 and 10, which are 50x60 mm in size an adapted specimen holder was used. Both samples also showed visible incidence of light from the top. To account for this effect, sample 9 was also tested with an additional cover, preventing the incidence of background light. Due to the location of the impact, the defect could not be centered in front of the camera for sample 10. After all samples had been tested, the first two measurements, comprising the reference sample and the normal impacted probe, were repeated. This was done to estimate the reproducibility of the experiments.

In front of the artificial sun, free floating room dust could be identified. Additionally, holding the reference sample against the light source it appeared scratched. These imperfections, though, were invisible in nominal light. The latter observation resulted in also marking the orientation of the reference sample, as an influence on the recorded images could not be ruled out. However, both previously mentioned effects should have little influence on the observed results, as the whole experiment is designed to identify relative differences between the samples and the described effects should average out. Fig. 4–6 and Fig. 4–7 show the original images from positions 1 and 2. Especially to the right and bottom of the satellite some structures of the laboratory are visible. This is in particular true in position 1, where the satellite only takes up a small area and the majority is black background.

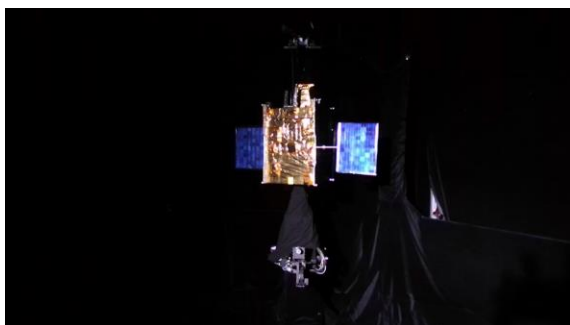


Fig. 4–6: Reference image in experiment position 1.

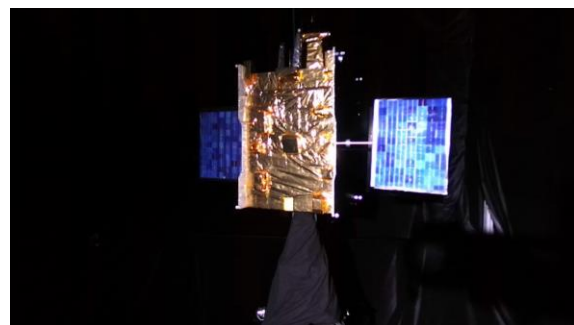


Fig. 4–7: Reference image in experiment position 2.

4.4.1.1 Evaluation

The depth images were filtered according to the depth and confidence, as described in section 3.1. Therefore, the confidence limit c_{lim} was set to 90 and the maximum depth value z_{max} was set to 4000 mm. After the filtering, approximately 6% of the pixels in position 1 and 16% of the pixels in position 2 have valid depth information. Table 4–4 holds the calculated precisions and accuracies in the two experiment positions. There is a clear difference in the two values for the two positions. The precisions are at 8 to 10 mm in position 1 and around 3 mm in position 2. Minor differences in these values exist between the different samples, however, all are within the scattering between the reference measurements at the beginning and the end of the experiment. A similar observation is made for the accuracy. The values in position 1 are at around

30 to 40 mm and between 10 and 12 mm in position 2. In contrast to the precision the accuracy of the reference measurement at the end is significantly smaller. The values are about half of the impacted samples and twice as high as the measurement precision. Yet, this value describes the error of measurement and is higher than expected. The existing differences in accuracy for the samples, therefore, are too small in comparison with the measurement error, to be considered.

Table 4–4: Precision and accuracy of variable glass experiment.

| Trial | Precision 1 [mm] | Accuracy 1 [mm] | Precision 2 [mm] | Accuracy 2 [mm] |
|------------|------------------|-----------------|------------------|-----------------|
| GRef | 9.9 | - | 2.9 | - |
| G0 | 10.3 | 41 | 3.0 | 10 |
| G01mm | 10.1 | 40 | 3.1 | 12 |
| G15 | 8.6 | 31 | 2.8 | 10 |
| G30 | 9.5 | 36 | 3.0 | 11 |
| G45 | 8.6 | 32 | 2.6 | 10 |
| G60 | 9.1 | 34 | 2.8 | 11 |
| G60Covered | 8.6 | 37 | 2.8 | 11 |
| G75 | 7.9 | 17 | 2.9 | 6 |
| GRef_End | 7.7 | 13 | 2.6 | 6 |
| G0_end | 9.3 | 45 | 3.1 | 11 |

Fig. 4–8 illustrates the relative accuracy as defined in section 3.3.1. The value is depicted above the impact angle. The red points are in position 1 and blue in position 2. The points mark the nominal trials, the crosses the control measurements at the end of the experiment, the squared ones the horizontal misplaced trial and the plus the trial with covers. There is no observable trend in the main series, however, some distinct observations can be made. In general position 1 produces smaller values compared to position 2. This is only violated for the 0° impact angle trials at the beginning and at the end. All values of the series are at around 3.5. The only outlier is the 75° impact angle sample, with a value below two, which is also the value for the comparison of both reference measurements. The figure illustrates the impact of displacing the sample and the uncertainty in repeating the trial. This already illustrates that the differences between the samples is smaller than the error of measurement, with contributing factors, such as moving the chaser, positioning the sample and covering the mount

from

incident

light.

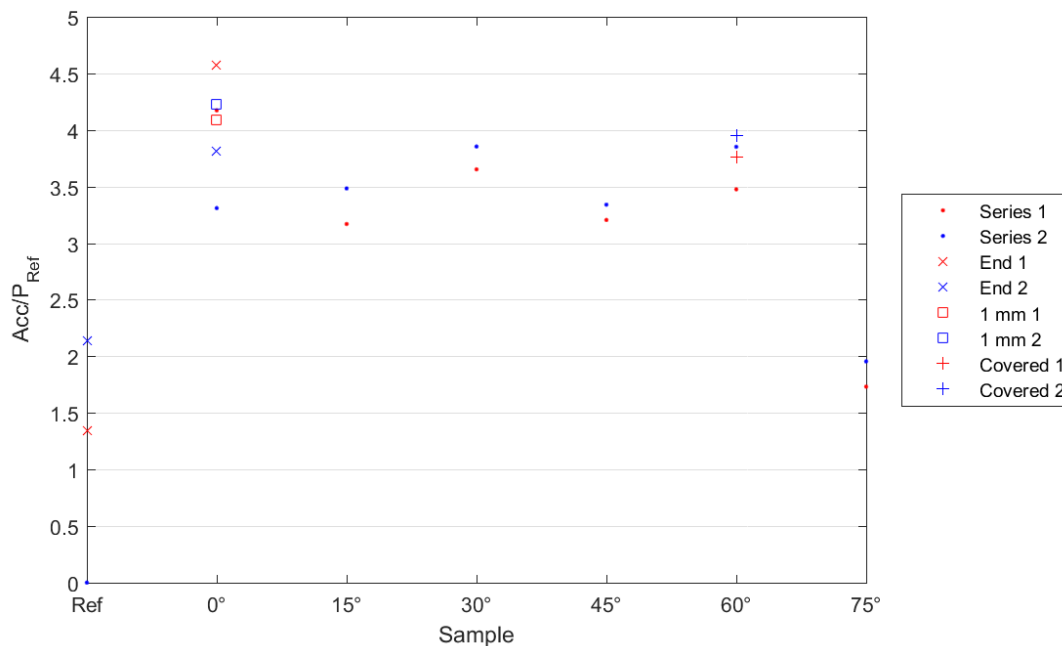


Fig. 4–8: Relative accuracy for glass with variable target distance.

Fig. 4–9 shows the depth densities as defined in section 3.4. The densities for the five possible categories are depicted above the impact angle. All densities are dimensionless values in between 0 and 1. The red data points represent experiment position 1 and the blue ones' position 2. Especially in the first graph, which gives the densities for no depth information in both images, there is a clear difference between the two experiment positions. Experiment position 1 has less depth information than position 2. Furthermore, there is no observable correlation with the impact angle. The second graphs gives the densities for pixels, where depth information is only available in the respective measurement, but not in the reference one. The values are around 5 per mill and no correlation with the impact angle is visible. Comparing this graph to the last one, which gives the densities for pixels, where depth information is only available in the reference measurement, there is clear similarity for the repeated reference measurement and the experiment position 1. However, the values for experiment position 2 clearly differ. The reason for this are unknown, but probably related to the position of the chaser platform. The third and the fourth graph give the densities of pixels, where both the reference and the disturbed measurement have depth information and the deviation between the depth values are within or beyond the reference precision. In general, the value for deviations greater than the precision is twice as high as for deviations within. This is only violated by the repeated reference measurement and the 75° samples, which are almost alike. At the same time this reveals the underlying error of measurement, as even in the best case only half of the pixels have deviations smaller than the reference precision.

The experiments with the glass samples proved the effect of the damaged optics on the depth perception. The relative accuracy was found to be approximately 3.5 for all samples. However, considering the repeatability of the experiment this value decreases to just below two. Furthermore, this quantity showed no correlation with the impact angle. The experiment proved the expected dependence of the precision and



accuracy from the distance to the recorded object. Yet, the effective evaluation could only be performed on 6% to 15% of the actual image area, as for the rest of the image no depth information was available after filtering.

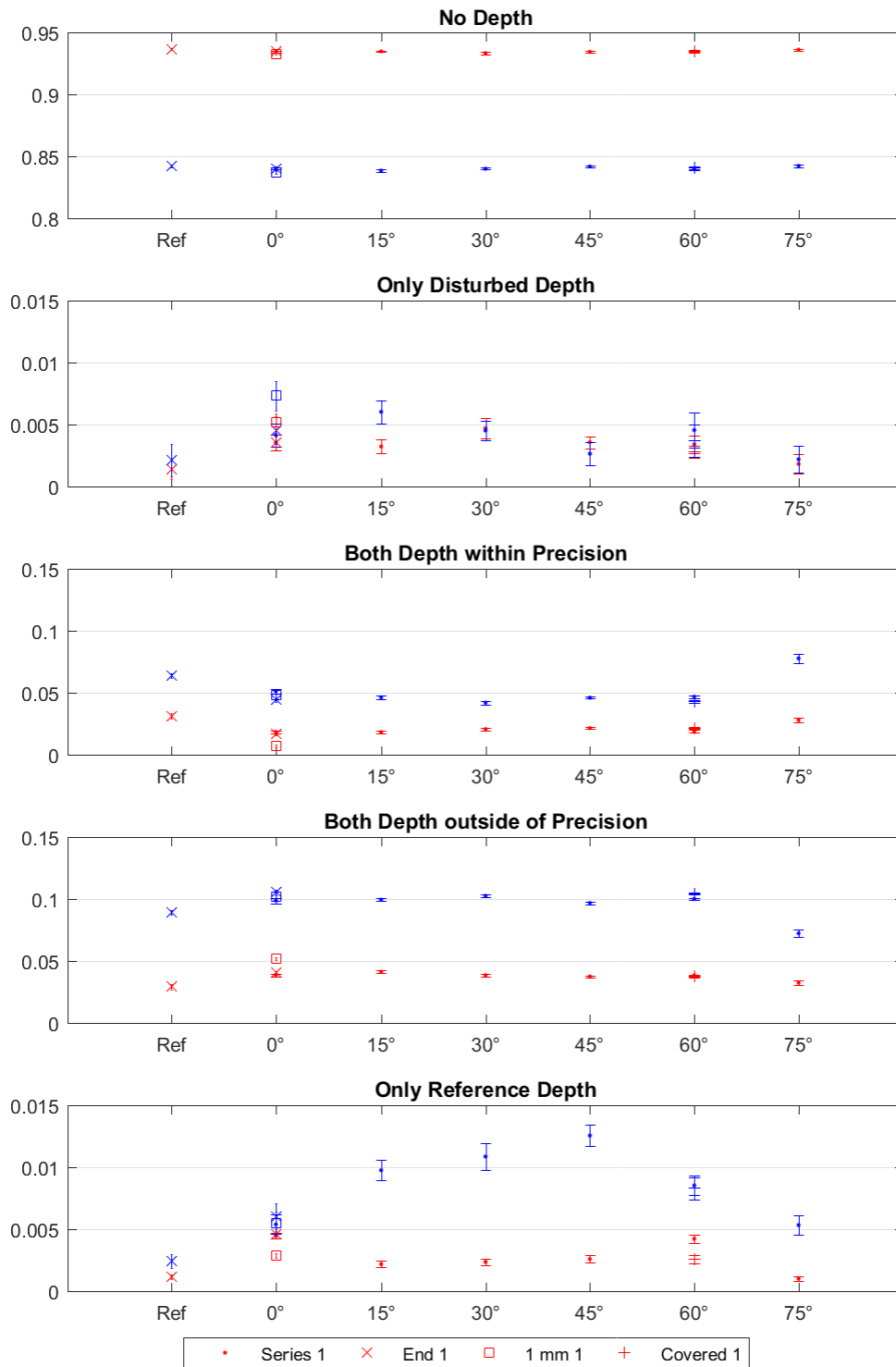


Fig. 4–9: Categorized depth densities for glass with variable target distance. The points marked in red are from experiment position 1 and the blue ones from position 2.

4.4.2 Makrolon®

For the second material, the mount had to be reassembled. Due to the material features, Makrolon® is much more scratch sensitive than the used silica glass. Large areas of the sample surfaces showed scratches due to the mounting in the particle accelerometer and the subsequent testing. As these defects are not equally distributed over the different samples, they would introduce additional noise and mismatch to the measurement. Therefore, the front plate with openings of 5 mm diameter was installed on the mount. This reduced the camera's field of view and the incident light and confined it to the impacted areas of the samples.

This experiment was conducted like the one described for glass in section 4.4. After the assembly of the mount, the laboratory was powered up. Then the camera script was started in auto mode. The resulting camera settings were then again fixed for the remainder of the experiment. This procedure surprisingly returned the same values as for glass, therefore Table 4–2 applies also for this experiment.

Subsequently the different samples were inserted into the mount and tested in position 1 and 2 (see Table 4–1). Unfortunately, only a subset of the samples could be tested in this configuration. This was due to variable burrs from beveling the samples, which prevented insertion into the mount. The sample orientation and displacement is found in Table 4–5. The orientation gives the position of the sample label as seen from the camera, which can be either top (T) or bottom (B) and left (L) or right (R).

Table 4–5: Sample orientation variable Makrolon®. Orientation is bottom (B), top (T), left (L), right (R).

| Trial | Sample Number | Orientation | Horizontal displacement [mm] | Vertical displacement [mm] |
|-------------|---------------|-------------|------------------------------|----------------------------|
| MRefAutoSet | MRef | BR | 0 | 0 |
| MRef | MRef | BR | 0 | 0 |
| M0 | 0M | TL | 2 | 1 |
| M45 | 13 | TL | 0 | 2 |
| M75 | 15 | TL | 0 | 0 |

For sample number 15 the larger specimen holder was used, as it is 50x60 mm in size. To prevent incident light from the top of the mount, it was covered with a cloth. As the repeatability of the measurements and the influence of the sample positioning were assumed universal, these measurements were not repeated.

Fig. 4–10 and Fig. 4–11 both show images of the scene, taken with the left camera. The dominating black background is due to the camera filming the backside of the mount's front. While the overall structure of the satellite is visible from position 1, the image taken in position 2 merely shows one side of the satellite.

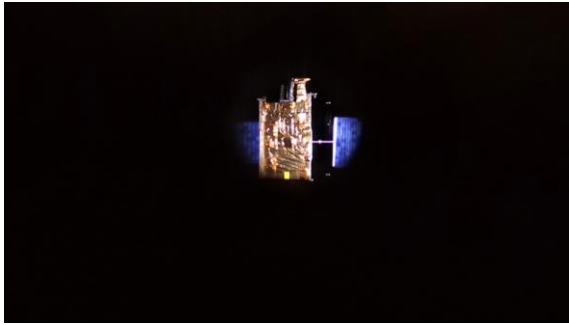


Fig. 4–10: Image of the left camera with limited field of view in position 1.

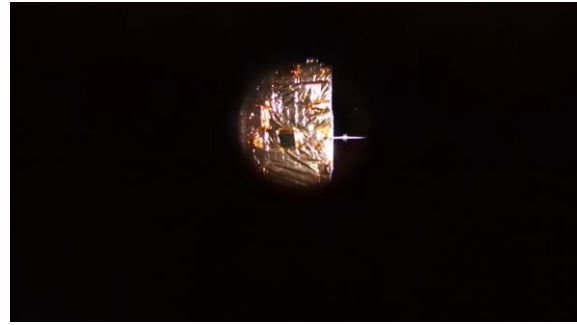


Fig. 4–11: Image of the left camera with limited field of view in position 2.

4.4.2.1 Evaluation

The maximum depth was set to $z_{\max}=4000$ mm and the confidence threshold to $c_{\text{lim}}=90$. After the filtering, approximately 3% of the pixels have valid depth information. This value is alike for both experiment positions. Table 4–6 holds the calculated precisions and accuracies for this experiment. The precisions in position 1 are around 9 mm and between 2 and 3 mm in position 2. The reference precision in the first position is considerably smaller with a value of 6.5 mm. The accuracies are around 40 mm and 10 mm for the two positions. Surprisingly, they are ordered with the impact angle, with higher angles leading to lower accuracies. This trend is confirmed in Fig. 4–12, which shows the relative accuracy above the samples. The value decreases with increasing angle and the difference between the two experiment positions also decreases with the angle. However, for this experiment only a subset of samples could be tested and no control measurement at the end of the experiment exists. Therefore, it is difficult to determine the error of measurement and inappropriate to support this trend. Considering the depth densities, there is no considerable difference between the two positions. This is possibly explained by the constant front opening, which is filled with satellite structure in both experiment positions (see Fig. 4–10 and Fig. 4–11).

While the experiment hinted at a possible correlation between relative depth accuracy and impact angle, this could not be verified. Yet, it proved the expected dependency of the accuracy from the distance to the observed object.

Table 4–6: Precision and accuracy of variable Makrolon® experiment.

| Trial | Precision 1 [mm] | Accuracy 1 [mm] | Precision 2 [mm] | Accuracy 2 [mm] |
|-------|------------------|-----------------|------------------|-----------------|
| MRef | 6.5 | - | 2.0 | - |
| M0 | 9.9 | 42 | 3.1 | 11 |
| M45 | 8.7 | 37 | 2.7 | 11 |
| M75 | 9.2 | 35 | 2.2 | 10 |

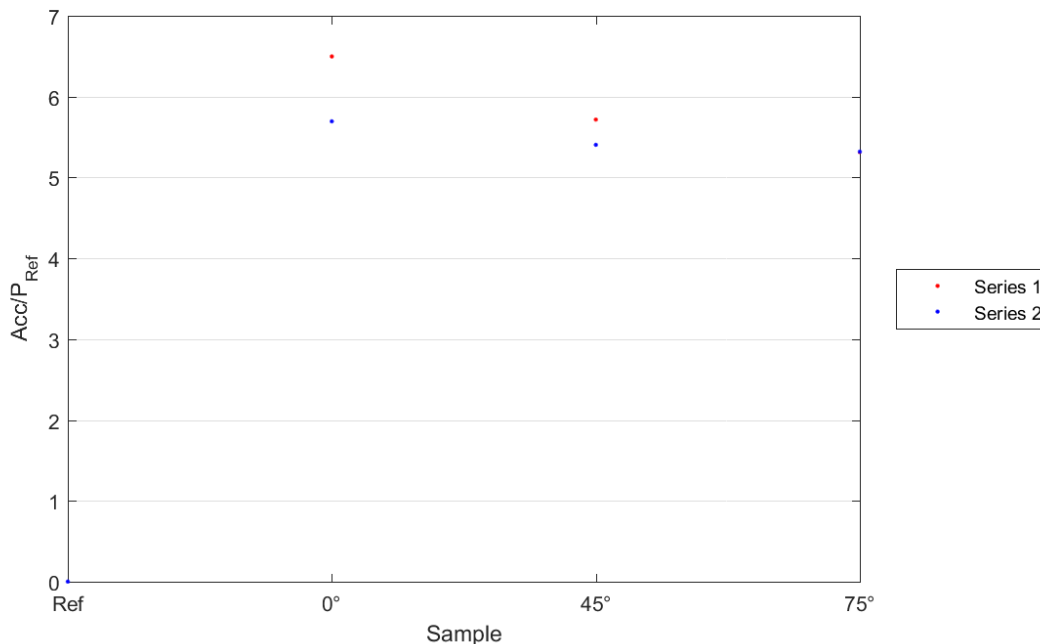


Fig. 4–12: Relative accuracy for Makrolon® with variable target distance.

4.4.3 Robustness of the Chaser Position

The positional displacement of the chaser platform, resulting from moving it, was identified as one possible source of error. To quantify this influence, the position of the chaser was recorded with the installed OptiTrack system [26]. Therefore, the experiment procedure was repeated, without recording images. The chaser was first brought in position 1, moved to position 2, returned to the sample exchange position and then again brought to positions 1 and 2. For each of the three axis the positions of two successive runs were recorded. Table 4–7 holds the coordinates along all three axes and the respective differences. These are in the magnitude of some millimeters. Taking the Euclidean distance between two successive points, results in 4.5 mm displacement in position 1 and 1.5 mm in position 2.

This test confirmed the positional variance of the chasers position, already described in [26]. The resulting variation of the camera position and the impact on the measurement is expected to be in the same order of magnitude. However, as the different position has not only an impact on the distance between camera and target, but also on the location of the target in the image, the true impact is unknown.

Table 4–7: Deviation of chaser position resulting from moving the platform.

| | Axis-1 [m] | Axis-2 [m] | Axis-3 [m] |
|--------|------------|------------|------------|
| Pos1_1 | -2.9843 | 2.2059 | 0.3894 |
| Pos1_2 | -2.9837 | 2.2103 | 0.3891 |
| Delta1 | 0.0006 | 0.0044 | 0.0003 |
| Pos2_1 | -1.5127 | 2.2351 | 0.3757 |
| Pos2_2 | -1.5116 | 2.2359 | 0.3752 |
| Delta2 | 0.0011 | 0.0008 | 0.0005 |

4.4.4 Conclusion

The expected dependency of the depth error and precision from the distance to the object could be shown. The measurements in position 1, which was further away from the target satellite shows a greater noise. The experiments showed a surprisingly high error of measurement. The exact source for this cannot be evaluated, yet it is probably a combination of different influencing factors. Moving the chaser platform already results in positional variation of some millimeters. Slight displacement of the mount or the sample can also have an influence. Comparing the two materials is not possible, as a different mount configuration was used. To allow comparison, a further experiment with the same configuration for both materials was conducted.

4.5 Fixed Distance from Target

To allow the comparison of both materials and to remove further disturbing factors another experiment was conducted. All remaining experiments were conducted with the mount with an opening of 5 mm in experiment position 2. Taking the closer position to the target should increase the measurement precision, which was confirmed in the previous experiment. Furthermore, it allows to move the chaser only along one axis, which could increase the accuracy of position. The z position of the chaser (axis 3) was moved in between -135500 and 0, to allow the exchange of the samples. The position of the other axes can be taken from Table 4–1 and were fixed during the experiments. To reduce incident light from the back a further cover was cut from black cardboard. Fig. 4–13 illustrates the covers, as well as the clamps, holding the samples to the mount. The clamps hold the black covers as well as the specimen holders, hidden below, to the mount. Underneath the right cover, the previously installed cardboard cover can be seen. It prevents the incidence of light through the split between camera and mount. The experiments used the same camera settings as in the previous ones, which can be retrieved from Table 4–2.

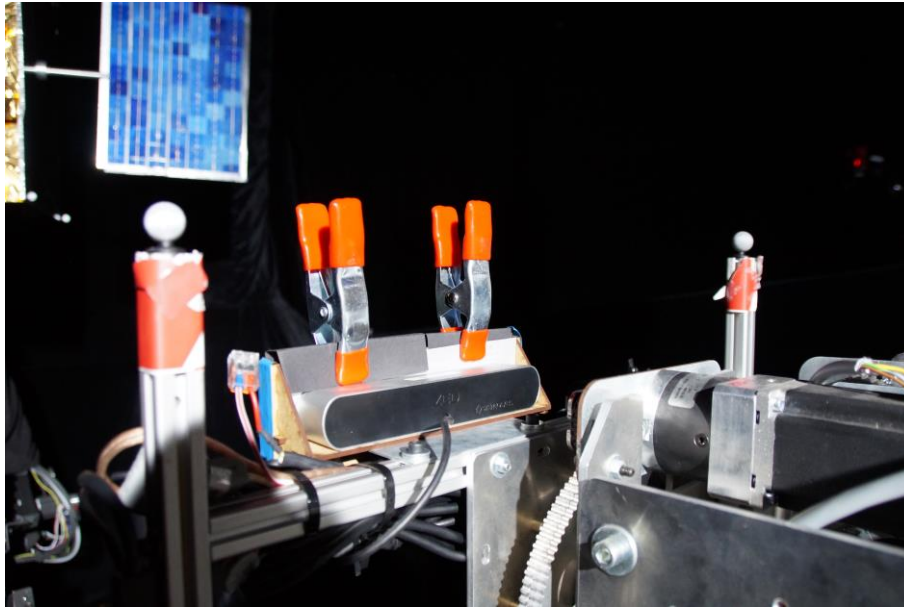


Fig. 4–13: Image of the experimental setup. The black cardboard covers prevent the incidence of light. The clamps hold the samples in position.

4.5.1 Glass

The glass experiments were repeated, to allow comparison with the Makrolon® experiments. Table 4–8 gives the trial names and the corresponding sample names in chronological order. First, the reference measurement was performed. Then, a set of glass samples, described in [6], with incidence angle of 0° was tested. This was done to evaluate the variance between different samples of the same angle. Following that, the samples with angles between 0° and 60° , described in [5], were tested. The 75° sample was omitted, as the defective area could not be brought in front of the lens. In the end, the reference measurement was repeated, to characterize the repeatability within the experiment and therefore also the measurement error.

Table 4–8: Sample orientation fixed glass. Orientation is bottom (B), top (T), left (L), right (R).

| Trial | Sample Number | Orientation | Horizontal displacement [mm] | Vertical displacement [mm] |
|----------|---------------|-------------|------------------------------|----------------------------|
| GRef | GRef | BR | 4 | 0 |
| Wear1 | 1G | TL | 0 | 0 |
| Wear2 | 3G | TR | 2 | 4 |
| Wear3 | 4G | TR | 0 | 2 |
| G0 | 0G | BL | 0 | 0 |
| G15 | 6 | TR | 6 | 3 |
| G30 | 7 | TL | 2 | 2 |
| G45 | 8 | TL | 3 | 0 |
| G60 | 9 | TL | 0 | 0 |
| GRef_End | GRef | BR | 4 | 0 |

Fig. 4–14 and Fig. 4–15 show images from the left camera taken for the glass measurements. The first one depicts the reference scene and the last one the measurement with the impacted glass at an angle of 15° . The well-defined border of the reference images is blurred for the impacted sample. This effect was visible for other samples to a varying degree.



Fig. 4–14: Image of the left camera for trial GRef.

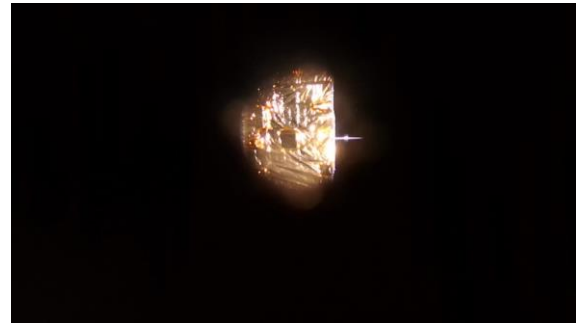


Fig. 4–15: Image of the left camera for trial G15.

4.5.1.1 Evaluation

As for the previous experiments the depth values were filtered according to the depth and confidence. The confidence limit c_{lim} was set to 90 and the maximum depth value z_{max} was set to 4000 mm. The filtering left 3% of the pixels with valid depth information. Table 4–9 holds the calculated precisions and accuracies. Since all experiments were conducted in position 2, the different values are for the two consecutive series, which were recorded. The deviation between two series is just some tenths of a millimeter. Noticeable is the difference in accuracy for the various samples of 0° impact angle. While the Wear1 and G0 sample have almost identical accuracies, the value of Wear3 differs by almost 3 mm. This observation can also be made in Fig. 4–16, which depicts the relative accuracy above the different samples. The red and the blue colored markers are from the two consecutive image series. The dotted values represent the nominal values, the crossed values originate from the reference measurement at the end and allow the estimation of the measurement error. Furthermore, the different markers at 0° represent measurements of the different 0° samples. The evolution of the nominal values above the impact angle show no clear tendency. Almost all values are within the interval spanned by the 0° samples. Taking the depth densities into account, the impacted samples have a slightly increased depth density compared to the reference measurement. At the same time the area, where only the reference measurement has depth information, increases slightly. These deviations, however, are in the magnitude of tenths of one percent. Considering this and the relative reference accuracy of 2, the experiments do not show a dependence of depth accuracy from the angle. However, the experiment confirms the effect, the impacted samples have on the depth measurements.

Table 4–9: Precision and accuracy of fixed glass experiment.

| Trial | Precision 1 [mm] | Accuracy 1 [mm] | Precision 2 [mm] | Accuracy 2 [mm] |
|----------|------------------|-----------------|------------------|-----------------|
| GRef | 1.9 | - | 1.9 | - |
| Wear1 | 2.1 | 12 | 2.2 | 12 |
| Wear2 | 2.3 | 11 | 2.5 | 10 |
| Wear3 | 2.2 | 9 | 2.3 | 9 |
| G0 | 2.6 | 12 | 2.5 | 12 |
| G15 | 2.2 | 8 | 2.1 | 8 |
| G30 | 2.1 | 9 | 2.2 | 10 |
| G45 | 2.6 | 14 | 2.6 | 14 |
| G60 | 2.2 | 11 | 2.1 | 12 |
| GRef_End | 1.9 | 4 | 2.0 | 4 |

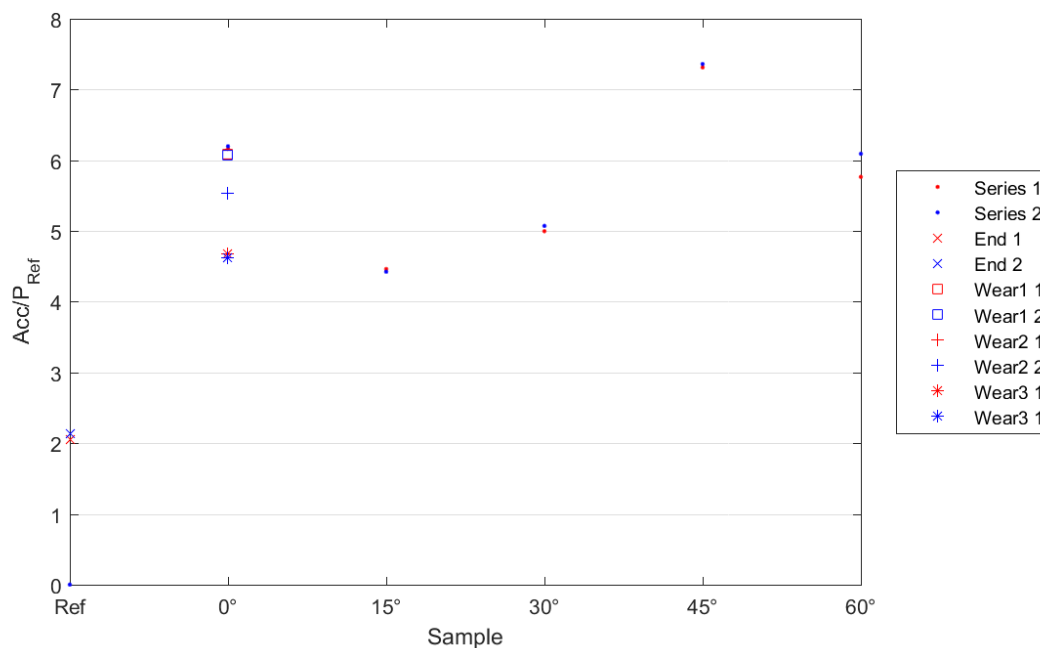


Fig. 4–16: Relative accuracy for glass with fixed target distance.

4.5.2 Makrolon®

As some of the Makrolon® samples had a burr from manufacturing, they were too large for the specimen holder (see section 4.4.2). Therefore, one holder was rasped up, to accommodate the samples. Since the variation, however, was not constant for all samples, this allowed a variable clearance between holder and sample. The following Table 4–10 shows the used samples, their orientation and the corresponding experiment name in chronological order. In the beginning, the reference trials were

performed. First, the samples were accidentally swapped between left and right, therefore, only the second reference experiment is to be considered as the real reference. This measurement was followed by the sample with incidence angle 0° . To characterize the positioning influence, a series of trials with horizontal displacement steps of 1 mm was performed. It was then followed by the samples up to an incidence angle of 75° . In the end, the reference measurement and the measurement of the 0° sample were repeated. As the reference sample was first inserted in the wrong placement (MRef_End), the trial was repeated as (MRef_End2). Finally, a measurement without any sample in the mount was performed. This was done to study the influence of placing the samples in front of the camera.

Table 4–10: Sample orientation fixed Makrolon®. Orientation is bottom (B), top (T), left (L), right (R).

| Trial | Sample Number | Orientation | Horizontal displacement [mm] | Vertical displacement [mm] |
|-----------|---------------|-------------|------------------------------|----------------------------|
| MRefR | MRef | BR | 0 | 0 |
| MRef | MRef | BR | 0 | 0 |
| M0 | 0M | TL | 2 | 1 |
| M01mm | 0M | TL | 3 | 1 |
| M02mm | 0M | TL | 4 | 1 |
| M03mm | 0M | TL | 5 | 1 |
| M15 | 11 | TL | 2 | 3 |
| M30 | 12 | TL | 1 | 2 |
| M45 | 13 | TL | 0 | 2 |
| M60 | 14 | BR | 2 | 0 |
| M75 | 15 | TL | 0 | 0 |
| MRef_End | MRef | BR | 2 | 1 |
| M0_End | 0M | TL | 2 | 1 |
| MRef_End2 | MRef | TL | 0 | 0 |
| M_without | - | - | - | - |

Fig. 4–17 to Fig. 4–20 show rectified images of the left camera, taken during the experiments. All images show the satellite structure in the center and a black background. This is due to the reduced opening of the sample mount, as for large areas of the image, the camera just observes the backside of the mount. Fig. 4–17 shows the reference image, Fig. 4–18 an image taken for the sample with an incidence angle of 75° . Fig. 4–19 and Fig. 4–20 both show images for the sample with an incidence angle of 0° , the first in the nominal position and the latter with a horizontal displacement of 3 mm. All the images, except for the reference, appear blurry. Noticeable are the stripes extending from the illuminated center into the dark background in Fig. 4–18. Similar effects could be observed for a few other samples. These can probably be explained by scattering of light from the defects, as no direct

incidence of light is possible outside the circled opening in the center. The borders in Fig. 4–19 and Fig. 4–20 appear even more blurry and especially in the last one, the satellite structure is hardly identifiable at all. Yet, in this measurement the scratches from handling the samples in the accelerometer were in front of the lens and not the impact site.



Fig. 4–17: Image of the left camera for trial MRef.



Fig. 4–18: Image of the left camera for trial M75.



Fig. 4–19: Image of the left camera for trial M0.



Fig. 4–20: Image of the left camera for trial M03mm.

4.5.2.1 Evaluation

The recorded data was evaluated using the respective script. Hereby, the confidence limit c_{lim} was set to 90 and the maximum depth value z_{max} was set to 4000 mm. The filtering left less than 3% of the pixels with valid depth information. Table 4–11 contains the calculated precisions and accuracies for the different trials and the two consecutive image series, recorded for every sample. The deviation between the two series is up to one millimeter. The reference measurements show precisions of around 2 mm. These values, however, get as high as 7 mm for the M03mm trial. The first trial MRefR shows a significantly smaller accuracy compared to the repeated reference measurements at the end of the experiment. In between this trial and the actual reference trial the two intact samples were swapped with each other.

Table 4–11: Precision and accuracy of fixed Makrolon® experiment

| Trial | Precision 1 [mm] | Accuracy 1 [mm] | Precision 2 [mm] | Accuracy 2 [mm] |
|-----------|------------------|-----------------|------------------|-----------------|
| MRefR | 1.9 | 4 | 2.0 | 4 |
| MRef | 2.5 | - | 2.5 | - |
| M0 | 3.0 | 19 | 3.1 | 18 |
| M01mm | 4.0 | 18 | 3.4 | 17 |
| M02mm | 4.4 | 17 | 4.3 | 17 |
| M03mm | 5.9 | 31 | 7.2 | 32 |
| M15 | 2.8 | 15 | 2.9 | 16 |
| M30 | 3.6 | 15 | 3.3 | 14 |
| M45 | 3.3 | 15 | 3.2 | 15 |
| M60 | 3.5 | 20 | 4.0 | 21 |
| M75 | 2.8 | 16 | 2.8 | 16 |
| MRef_End | 2.5 | 7 | 2.2 | 7 |
| M0_End | 3.3 | 14 | 3.3 | 14 |
| MRef_End2 | 2.1 | 8 | 2.1 | 7 |
| M_without | 1.9 | 10 | 1.8 | 10 |

Fig. 4–21 shows the relative accuracy above the impact angle. The red and blue marked values derive from the two consecutive measurements of the same scene. The dotted values depict the nominal measurement series. The crossed values are the control measurements at the end of the experiment. The other values for the 0° impact angle illustrate the variation coming from horizontal displacement of the sample. There is no visible correlation between the impact angle and the relative accuracy. Especially, if the repeated measurements at the end and the displacement measurements are considered. However, the 60° sample and the 3 mm displaced 0° sample show a significant peak. The latter is probably explained by the secondary damages on the samples. The 3 mm displacement centered these scratches in front of the lens. The other displaced trials show a slight trend, where the relative accuracy decreases with increasing displacement. This suggests that the damaged area could be centered in front of the opening, as with deviation from this position the accuracy decreases first, before it increases again, due to the secondary damages. Yet, this trend could be just coincidental.

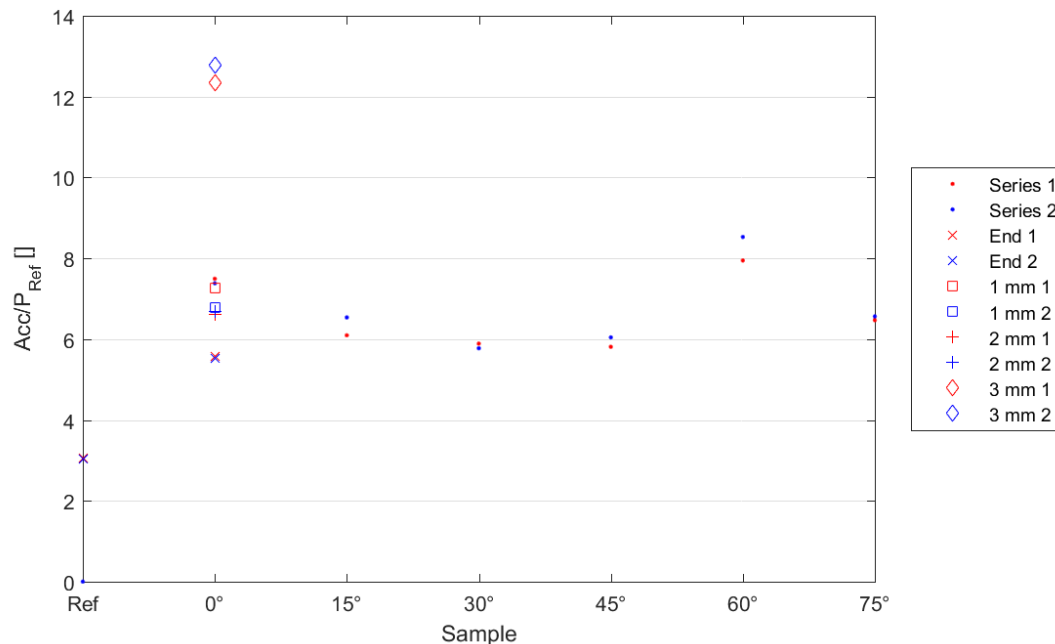


Fig. 4–21: Relative accuracy for Makrolon® with fixed target distance.

This experiment also showed a great uncertainty, which is visible for the measurements at the end. The repeated reference measurement MRef_End2 deviates from the initial reference measurement by three times the reference precision. Comparing the reference with the previously conducted trial MRefR this value decreases to 1.6, which is almost half the value at the end. This implies the following conclusions. In contrast to two consecutive image series (see section 4.3), the relative accuracy between two consecutive trials does not reach values below one. It suggests an existing error of measurement resulting from moving the chaser, exchanging the samples or restarting the camera. With increasing number of trials the error seems to be variable, which could be caused by single disturbing effects, such as a slight misplacement of the sample mount. The factors are supported by a visual study on the images of the right camera, which revealed that the image section differs slightly from image to image. Furthermore, the hue of the satellite structure looks slightly different for reference images and ones with impacted samples. The reason for this is unknown, especially since the camera settings were controlled to be the same and the sample in front of the right camera was not changed at all.

The depth densities also do not show an observable trend. Only the M03mm trial shows a distinct behavior, as it has a large fraction of pixels with lost depth information, compared to the reference measurement.

The experiment could not show a correlation between impact angle and depth accuracy. Yet it proved the influence of the defective samples on the accuracy. This value is 6 times higher than the reference precision and still 2 times higher than the accuracy of the repeated reference measurement.

5 Discussion

The experiments show that the particle impacts have negative effects on the depth measurement. Unfortunately, a correlation between the incidence angle of the impact and the quality of the depth measurement could not be shown. Still, a possible relation cannot be ruled out, as the experiments show a significant error of measurement and the deviations between the samples are within this error. The following section discusses the findings of the experiments, the shortcomings and possible improvements. The subsequent section then addresses the applicability of the tested scenario to real missions.

5.1 Experiments

The experiments proved a noteworthy influence of defected optics on the performance of the stereo vision camera. The relative accuracy is in average between 5.5 and 6.5 for all experiments, except for the glass samples with variable distance, which has a value of 3.5. This can partly be explained with an increased value for the reference precision in this experiment, which is probably linked to the different mount configuration. Having a larger front opening, this results in a broader field of view. The smaller opening, used in the other experiments, just allows the recording of the front side of the target. This is supported by the overall depth density. The experiments with the reduced front opening, all have densities of 3% after the filtering process. Noticeable is that there is no difference in the density for variable distance to the target with the reduced opening and the Makrolon® samples. The experiment with the broad opening and glass in contrast has densities of 6% in position 1 and 16% in position 2 after the filtering process.

All experiments show a poor repeatability, since the deviation between reference measurements at the beginning and the end of the experiments result in relative accuracies ranging from 1.5 to 3. Two successive reference measurements, where the sample was swapped in between (see section 4.5.2.1) resulted in a deviation of approximately 1.5, on the one hand. On the other hand, two independent reference measurements at the end, separated by just one other, have an almost equal value of three. These observations lead to the following conclusions. Firstly, there is already a distinct error, resulting from moving the chaser platform in between the trials. Secondly, there seems to be an error caused by single events, such as slight shifts of the mount, produced during the exchange of the samples. Indeed, the position variance of the chaser was proven by measuring its position in two consecutive runs (see section 4.4.3), which produced a displacement of one to four millimeters. Since this is split in all three axis dimensions, it does not only alter the distance of the camera to the target, but also the image section in which the target appears. An experiment to narrow down the contribution of this factor would be a test series, where either the chaser is moved without changing the samples, or the chaser's position is fixed and the samples are exchanged.

An additional source of noise is caused by the placement of the samples. The mount was designed to ensure that the perfectly centered impact is in front of the lens, without any displacement of the specimen holder. However, the impact sites are scattered around this center by up to 5 mm in each axis, which made a variable placement necessary. The most affected area of the impact had to be manually centered in front

of the lens to compensate for this scattering. To make this manual intervention reproducible the following measures were taken: A scale with millimeter resolution was engraved to the mount and allowed the determination of horizontal placement. The vertical placement was achieved with polystyrene plates of 1 mm thickness, which were brought between mount and specimen holder. As the horizontal position is determined visually from the scale, errors of tenths of millimeters are possible. The vertical displacement in contrast can be considered accurate. However, the plates separate the specimen holder from the horizontal scale, which results in higher uncertainty along the horizontal axis. To eliminate this manual influence, it would be necessary to insert all samples in the defined position, marked by the stop. This would, however, call for the samples to be inserted in the same defined position in the accelerometer. Furthermore, the number of samples per impact scenario would have to be increased. Only then it is plausible for the random scattering to be averaged out. The noticeable difference between samples with equal impact angle 0° was shown in the experiment with glass and fixed target distance (see section 4.5.1). It should be noted that the samples in this experiment were placed manually, as their orientation in the accelerometer could not be reproduced. Additional control measurements with horizontally displaced samples showed a considerable influence on the accuracy. Especially for the Makrolon® samples, where secondary damages are close to the impacted areas this effect is pronounced. Measuring these secondary defects results in accuracies twice as high as the ones from the particle impacts. This confirmed the need for the reduced front opening to cover the secondary defects.

The effect of the sample position on the measured performance could be enhanced by the observed scene itself. The target satellite takes up only a small area of the complete image, while the majority is the black curtain of the laboratory. The same is applicable for the mount with the reduced front opening. Most parts of the images are covered by the mount and, therefore, dark. Because of the principle of stereo vision, the camera is unable to generate reliable depth information in these dark and textureless areas. This results in 85% to 97% of the image having no depth information after the filtering process and the metrics are only calculated with 3% to 16% of the image. The precision just takes pixels into account, which have a valid depth information (value greater than zero). For calculation of the accuracy the corresponding pixel needs to have valid information in both compared images, which reduces the considered portion even further.

The position of the defects has a fundamental influence on the calculated result. If the most affected area is placed above the black background its effect on the accuracy will be negligible. This is because the reference measurement already has no depth information in these areas, which prevents the calculation of the accuracy right from the start. A possible experiment to classify this effect would be to rotate the chaser around the vertical axis with fixed sample position. Thereby, the target satellite would appear in different areas of the image, which are differently affected by the particle impacts. The effect could be reduced if the complete scene could be measured by the camera, which would need a brighter background with more texture. This would lead to an increased depth density and allow for a better comparison between the images, as the metric variables can only be calculated on parts of the images with at least one of the two compared images having valid depth information.

The slightly changing image section poses further noise on the accuracy and the depth densities. While the precision is calculated from a series of images in one trial, the

accuracy and depth densities are calculated between two trials, where the chaser has been moved. This results in a slight shift of the camera and the target within the image. However, the accuracy compares corresponding pixels in both images, ignoring the possible shift of an object. The same is true for the calculated depth densities, which compare the depth values of two corresponding pixels and classify the differences to the five categories. Yet, if the position of the target changes within the image frame, two pixels cannot be expected to have the same depth value. Especially at depth discontinuities, such as borders of the satellite this has a noteworthy influence. The effect is predominately visible in the densities and explains why even for two reference measurements only half of the pixels with depth information in both images are within the precision. The shift of the target position also explains the comparable density values for pixels having depth information only in either the reference or the defective. Additionally, the shift of the target position in the image frame probably explains the noteworthy accuracy values between different reference measurements.

Another issue is the size of the impact areas. The lower the impact angle the wider the affected area. This is also one reason for the larger sample size for 60° and 75° impacts. Placing the samples directly in front of the camera allowed only parts of the impacted areas to be investigated. This problem is increased by the reduced opening of the mount, which allows only a narrow part of the impact area to be investigated. Especially for the samples with high impact angles, it was difficult to determine a reasonable position. For the 75° glass sample, it was even impossible to center the defect in front of the camera. Since the investigated area is selected manually this introduces a potential bias. The situation could be improved by putting the samples further away from the camera to have a greater portion of the sample inside the cameras' field of view. However, this would increase possible reflections on the backside of the samples and the sample borders and mount could get into the camera's field of view, disturbing the measurement. The reflection of background light was already a problem in the current experiments. Cardboard covers were used to reduce the amount of incident light, however, they did not completely shield the mount. Another cover to completely protect the mount from background light should, therefore, be used in further experiments.

An additional source of noise, solely related to the Makrolon® samples is their variable burr. The specimen holder had to be rasped up to accommodate the samples. Yet, this allows clearance within the holder for samples with a smaller burr and adds further uncertainty. To avoid this disturbance in future experiments, the sample size should be as uniform as possible and the samples should be rasped to a uniform size before the impact experiments are conducted.

The conducted experiments proved the negative influence of dust impacts on the performance of a stereo vision system. Yet, the noteworthy error of measurement just allows general conclusions to be drawn. This error can be partially explained by introduced noise from the experiment setup. Further experiments should minimize this influence and avoid disturbing factors, such as moving the chaser. Additionally, the mount and the fastening to the chaser should be reevaluated to increase repeatability and prevent dislocation. The assessment of the performance could be improved by using information on the ground truth. This would allow a true assessment of the systems' performance instead of the relative comparison, used in the present work. The present work solely relies on the assumption that the reference measurement is true and the best possible solution.

Further sources of noise are the manual intervention, caused by placing the samples and selecting the investigated impact region. The secondary damages, especially present on the Makrolon® samples cause further disturbances. Therefore, these damages should be avoided.

5.2 Application of Scenario

The scope of the present work was to study the influence of dust impacts during proximity operation of two spacecraft. The RACOON laboratory provided the necessary environment. Yet, differences to the true space environment conditions occur. The absence of vacuum in the laboratory should have no influence on the overall performance of a stereo vision system. Furthermore, disturbing factors such as floating dust in the air and already existing imperfections on the camera should have averaged out. The simulated sun, however, has a matching spectrum, but a significantly decreased intensity. This could have influence on the reflections caused by the satellite or the impacted particles.

A further concern is the tested scene. The accuracy of the camera was just evaluated for one specific scene, with fixed orientations of the sun, the target and the chaser. In a real application, however, these conditions will be permanently changing. In addition, the real applications will not rely on only one image of the scene to be recorded, but on a series. The aim is then to reconstruct the targets shape and movement. Therefore, other metrics, quantifying the capability of achieving these goals could be used to evaluate the performance in nominal and degraded conditions. This would improve the applicability of the drawn conclusions. Then it would be possible to determine if the actual mission could still be achieved with degraded optics, which is the actual problem to be investigated. If this is found to be not the case, preventive measures would have to be taken. These are for example, the usage of baffles and shields to reduce or prevent impacts, or the usage of redundant systems to compensate failures. One such option could be a third camera, allowing the drop out of one.

The biggest concern with the tested scenario, however, is the used samples. They were created with moon simulant material and at velocities of 360 m/s. The interplanetary dust particles and debris particles are expected to impact with velocities of more than 10 km/s. Yet, slower particles cannot be ruled out, as these velocities are average values. Unfortunately, it was infeasible to test higher impact velocities and at too high velocities an impact could also destroy the complete camera, making further recordings impossible. Additionally, the samples were impacted with a defined mass, equivalent to multiple particles. While this could be possible, especially for impacts of secondary ejecta, single particle impacts could have different effects. Investigating these single events could also reduce problems of the experiment setup, as the affected areas are likely smaller and can be placed more reliably in front of the actual target. Instead of the impact angle, particle velocity and number could be varied and correlations with the stereo vision performance investigated.

6 Conclusion

The aim of the present work was to study the influence of dust impacts on the performance of a stereo vision system. A possible correlation of performance and impact angle should be investigated. To address these questions, an experiment was set up, using various optical samples, intact and impacted, which were placed in front of a stereo vision camera in the RACOON laboratory. The laboratory provided the environment to simulate orbit conditions. By comparing measurements with defective samples to a common reference, the relative performance of the stereo system was evaluated. Deviations in terms of precision, accuracy and relative depth densities were evaluated. Two different materials, glass and Makrolon®, were tested and a relative accuracy (accuracy divided by reference precision) between 3 and 6 was found. A correlation of this value with the impact angle could not be identified. One plausible reason is the surprisingly high error of measurement, which can be partly tracked down to the positional robustness of the laboratory. The chaser with the attached camera was moved between the experiments, resulting in slight misplacements. Additionally, the observed scene is challenging for the unimpaired stereo camera already, as most of the image is black background and the illuminated target satellite tends to have distinct reflections. Furthermore, the impacts on the samples are scattered around the center, which made it necessary to manually select and place the most affected area in front of the lens. To overcome these problems, a set of further experiments has been proposed, especially regarding the reduction of the error of measurement. For this purpose, the camera position should be kept constant, even though this makes the exchange of the samples more difficult.

The applicability of the realized experiments is limited. The samples used, were impacted with significant lower velocities than are expected from in orbit dust impacts. Additionally, the samples featured multiple instead of single impacts. Future work should, therefore, focus the following tasks: Firstly, representative samples should be defined and generated. Secondly, the impact experiments should be conducted in a way to reduce the necessity of manual intervention in the stereo vision experiments. For example, secondary damages, present in the Makrolon® samples, should be avoided. If this is not possible, investigation should focus on the silica glass, which is less prone to scratches.

A further concern lies in the used metrics. The calculation was only possible on small parts of the images, as for most areas no depth information was available, due to the black background. This could be improved by using a generic background, providing depth information for most parts of the images. However, this would reduce the comparability with the environment conditions. At the same time, the experiments only investigated single scene images, while the real application includes a series of measurements with changing orientations. The actual goal of the depth measurements is the generation of surface models of the target and the extraction of its motion. Using metrics to assess the quality of this processed information could increase the applicability of the results to the actual task.

Despite relevant discrepancies between laboratory and in-orbit conditions, this work represents a first approach to study the relevance of dust impacts on camera optics during proximity range operations. Further studies should focus more on the generation of representative samples and consider the implications on the experiments and the error of measurement.

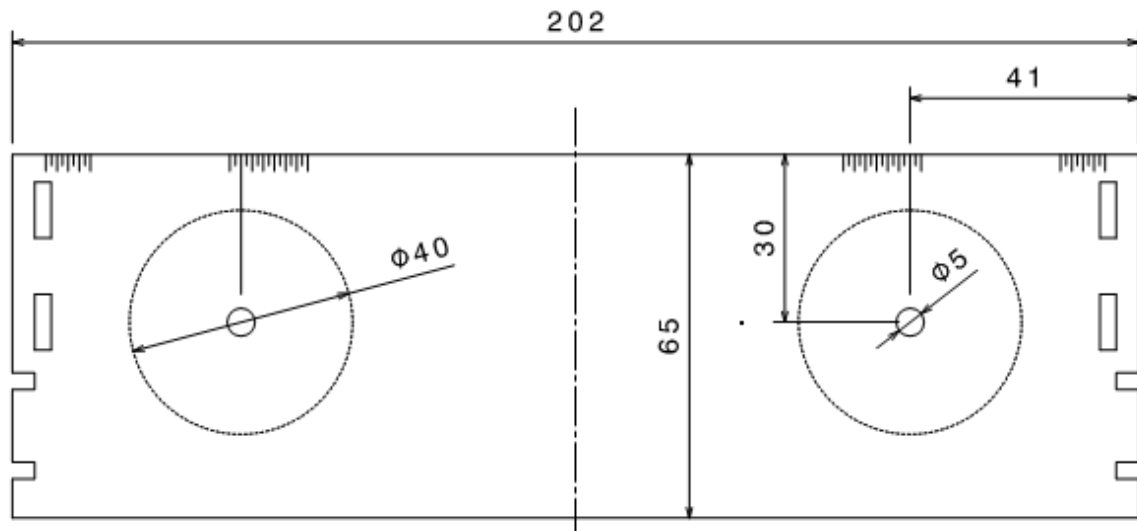
7 References

- [1] D. Whitlock *et al.*, “The Characteristics and Consequences of the Break-up of the Fengyun-1C Spacecraft,” *58th International Astronautical Congress*, <https://ntrs.nasa.gov/archive/nasa/casi.ntrs.nasa.gov/20070007324.pdf>, 2007.
- [2] J. N. Pelton, *New Solutions for the Space Debris Problem*. Cham [u.a.]: Cham [u.a.]: Springer International Publishing, 2015.
- [3] D. Fourie, B. E. Tweddle, S. Ulrich, and A. Saenz-Otero, “Flight Results of Vision-Based Navigation for Autonomous Spacecraft Inspection of Unknown Objects,” *Journal of Spacecraft and Rockets*, vol. 51, no. 6, pp. 2016–2026, 2014.
- [4] Edward M. Silverman, *Space environmental effects on spacecraft: LEO materials selection guide, part 1 - NASA-CR-4661-PT-1*, 1995.
- [5] C. A. Bühler, “Experimentelle Untersuchung der Schadwirkung von Staubeinschlägen unter verschiedenen Winkeln während Lunaren Landevorgängen,” in *Deutscher Luft- und Raumfahrtkongress 2015*, 2015.
- [6] C. A. Bühler, “Experimental investigation of lunar dust impact wear,” *Wear*, vol. 342-343, pp. 244–251, 2015.
- [7] G. Drolshagen, “Hypervelocity impact effects on spacecraft,” in *Meteoroids 2001 Conference*, 2001, pp. 533–541.
- [8] A. L. Graps *et al.*, “GEO Debris and Interplanetary Dust: Fluxes and Charging Behavior,” *Dust in Planetary Systems*, vol. 643, pp. 97–102, 2007.
- [9] G. Sansoni, M. Trebeschi, and F. Docchio, “State-of-The-Art and Applications of 3D Imaging Sensors in Industry, Cultural Heritage, Medicine, and Criminal Investigation,” (eng), *Sensors (Basel, Switzerland)*, vol. 9, no. 1, pp. 568–601, 2009.
- [10] L. Matthies *et al.*, “Computer Vision on Mars,” *Int J Comput Vis*, vol. 75, no. 1, pp. 67–92, 2007.
- [11] J. Maki *et al.*, “The Mars Science Laboratory Engineering Cameras,” *Space Sci Rev*, vol. 170, no. 1-4, pp. 77–93, 2012.
- [12] R. Willson, M. Maimone, A. Johnson, and L. Scherr, “An optical model for image artifacts produced by dust particles on lenses,” in *‘i-SAIRAS 2005’ - The 8th International Symposium on Artificial Intelligence, Robotics and Automation in Space*, 2005, p. 103.1.
- [13] *ATV-5 set to test new rendezvous sensors*. [Online] Available: http://www.esa.int/Our_Activities/Human_Spaceflight/ATV/ATV-5_set_to_test_new_rendezvous_sensors. Accessed on: Jun. 06 2017.
- [14] K. van Hecke *et al.*, “Self-supervised learning as an enabling technology for future space exploration robots: ISS experiments,” *67th International Astronautical Congress*, <http://www.esa.int/gsp/ACT/doc/AI/pub/ACT-RPR-AI-2016-IAF-selfsupervisedlearningontheISS.pdf>, Sep. 2016.

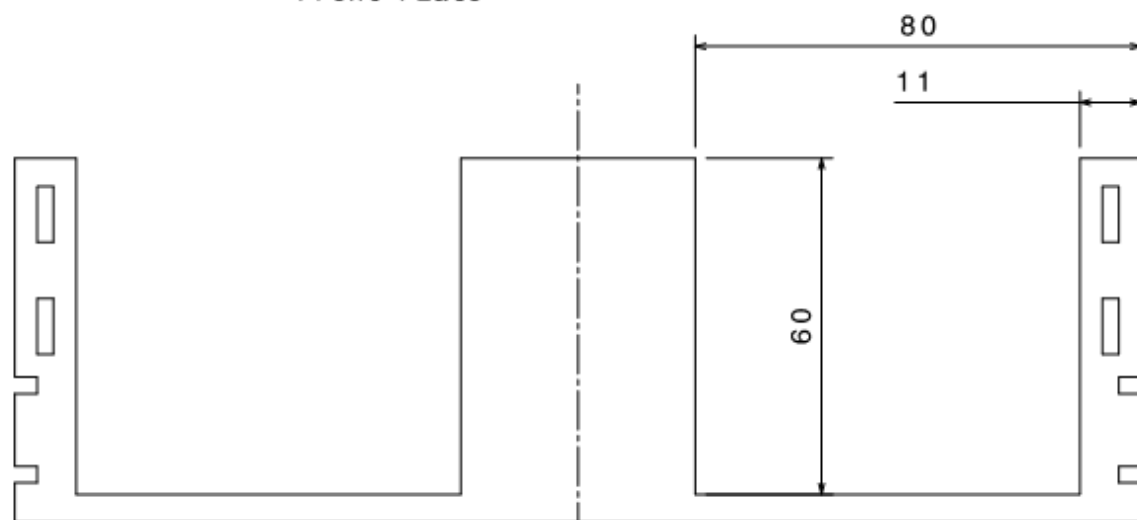
- [15] A. Ciadamidaro, "Auslegung und Konstruktion eines Sonnensimulators für eine Simulationsumgebung zur Nahbereichsnavigation von Satelliten," Bachelor's Thesis, Institute of Astronautics, Technische Universität München, Munich, 2016.
- [16] Stereolabs, *Stereolabs SaveDepth*. [Online] Available: <https://github.com/stereolabs/zed-examples/blob/master/depth%20sensing/src/SaveDepth.cpp>. Accessed on: Jun. 06 2017.
- [17] Stereolabs, *Stereolabs Zed-Opencv*. [Online] Available: <https://github.com/stereolabs/zed-opencv/blob/master/src/main.cpp>. Accessed on: Jun. 06 2017.
- [18] Stereolabs, *ZED Advanced Settings*. [Online] Available: <https://www.stereolabs.com/documentation/overview/depth-sensing/advanced-settings.html>. Accessed on: Jun. 06 2017.
- [19] *ZED SDK 2.0.0*. [Online] Available: <https://www.stereolabs.com/developers/release/2.0/>. Accessed on: Jun. 06 2017.
- [20] J. J. Rodriguez and J. K. Aggarwal, "Quantization error in stereo imaging," in *Proceedings CVPR '88: The Computer Society Conference on Computer Vision and Pattern Recognition*, pp. 153–158.
- [21] C. D. Mutto, "TOF Cameras and Stereo Systems: Comparison and Data Fusion," in *TOF Range-Imaging Cameras*, F. Remondino and D. Stoppa, Eds., Berlin, Heidelberg: Springer Berlin Heidelberg, 2013, pp. 177–202.
- [22] D. Scharstein and R. Szeliski, "A Taxonomy and Evaluation of Dense Two-Frame Stereo Correspondence Algorithms," *International Journal of Computer Vision*, vol. 47, no. 1, pp. 7–42, 2002.
- [23] D. Scharstein, R. Szeliski, and H. Hirschmüller, *Middlebury Stereo Vision*. [Online] Available: vision.middlebury.edu/stereo/. Accessed on: Jun. 06 2017.
- [24] J. Gu, R. Ramamoorthi, P. Belhumeur, and S. Nayar, "Removing image artifacts due to dirty camera lenses and thin occluders," in *ACM SIGGRAPH Asia 2009 papers*, p. 1.
- [25] S. Song, S. P. Lichtenberg, and J. Xiao, "SUN RGB-D: A RGB-D scene understanding benchmark suite," in *Proceedings of the 28th IEEE*, pp. 567–576.
- [26] J. Otto, "Development of an Absolute Reference Measurement System in the Racoon Hardware Lab," Masters's Thesis, Institute of Astronautics, Technische Universität München, Munich, 2017.

A Appendix

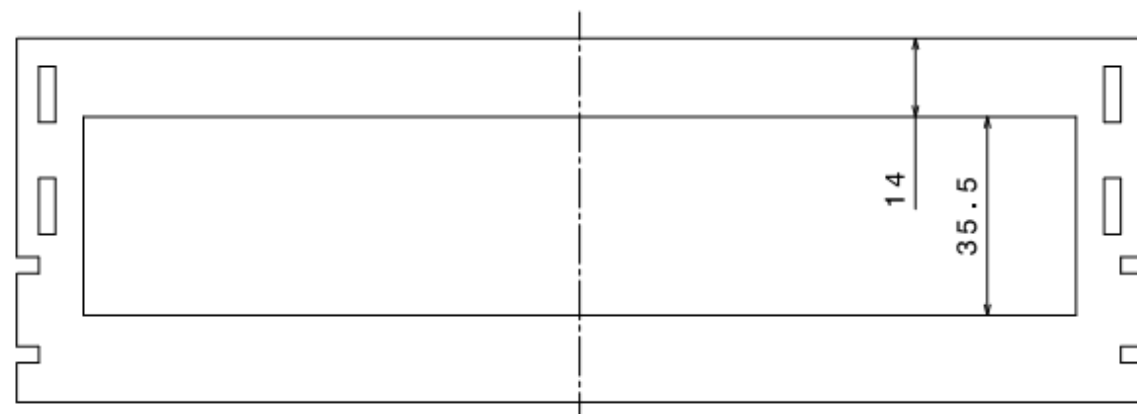
A.1 Production Drawings



Front Plate

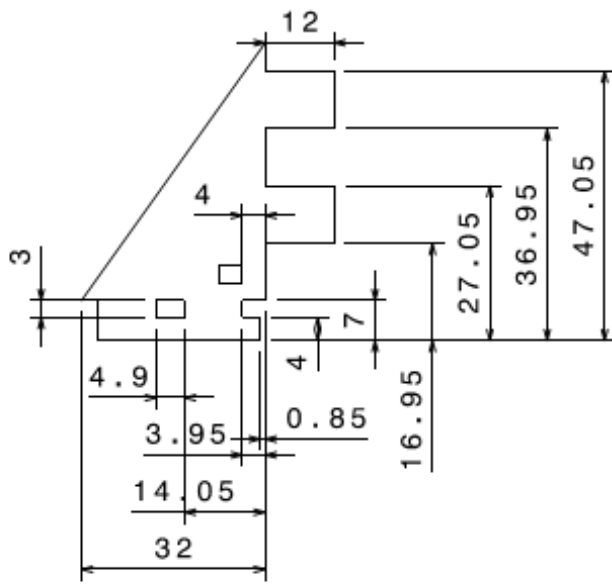
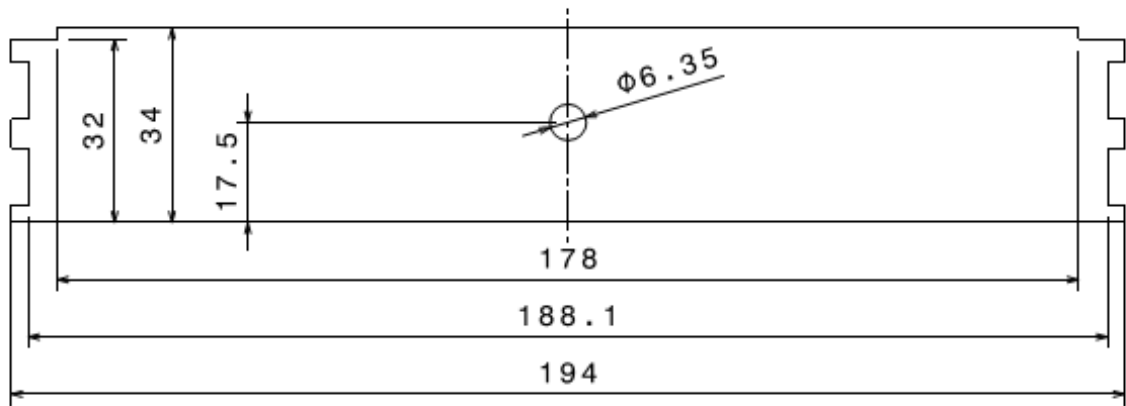


Middle Plate

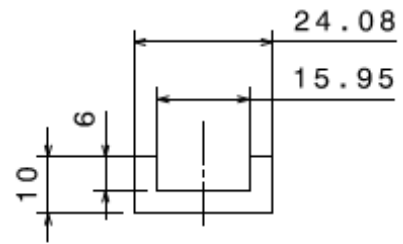


Back Plate

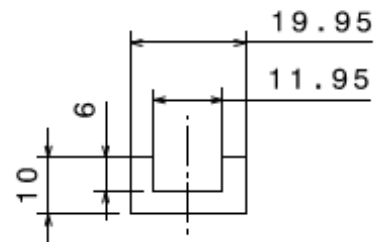
Base Plate



Side Panel

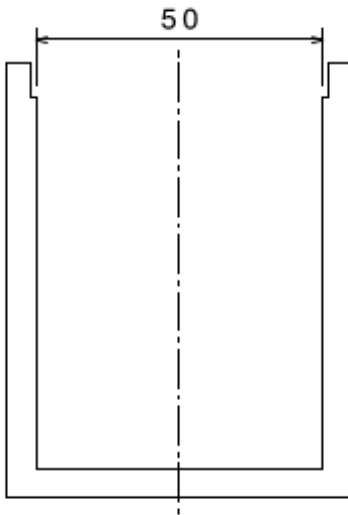
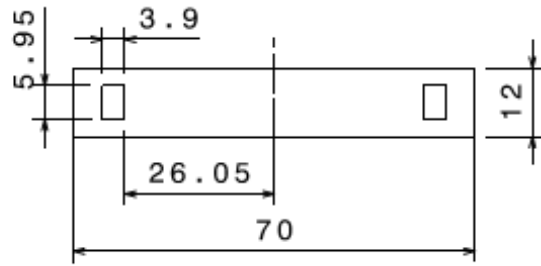


Connector 1

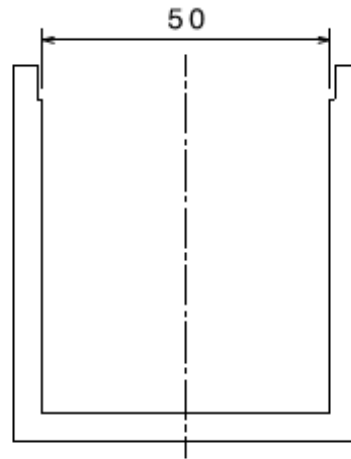


Connector 2

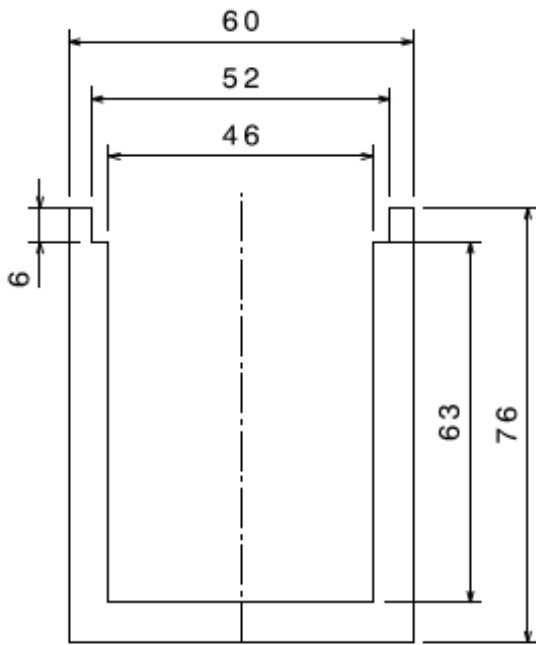
Holder Connector



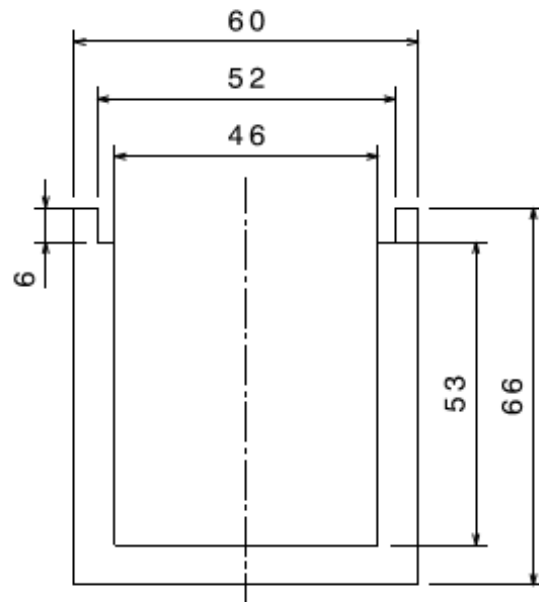
Large Holder 2



Small Holder 2



Large Holder 1



Small Holder 1

A.2 Categorized Depth Densities

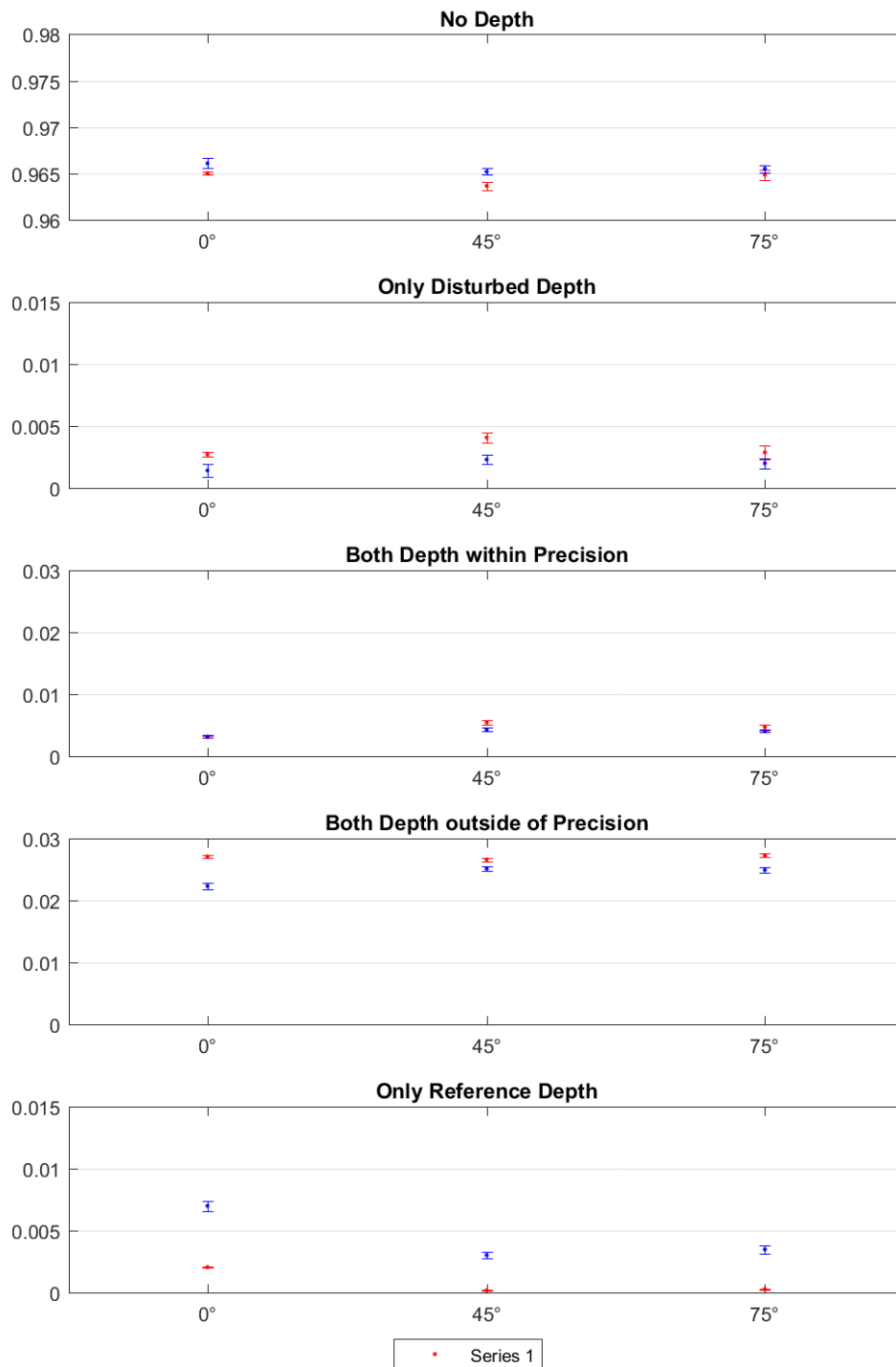


Fig. 6–1: Categorized depth densities for Makrolon® with variable target distance. The points marked in red are from experiment position 1 and the blue ones from position 2.

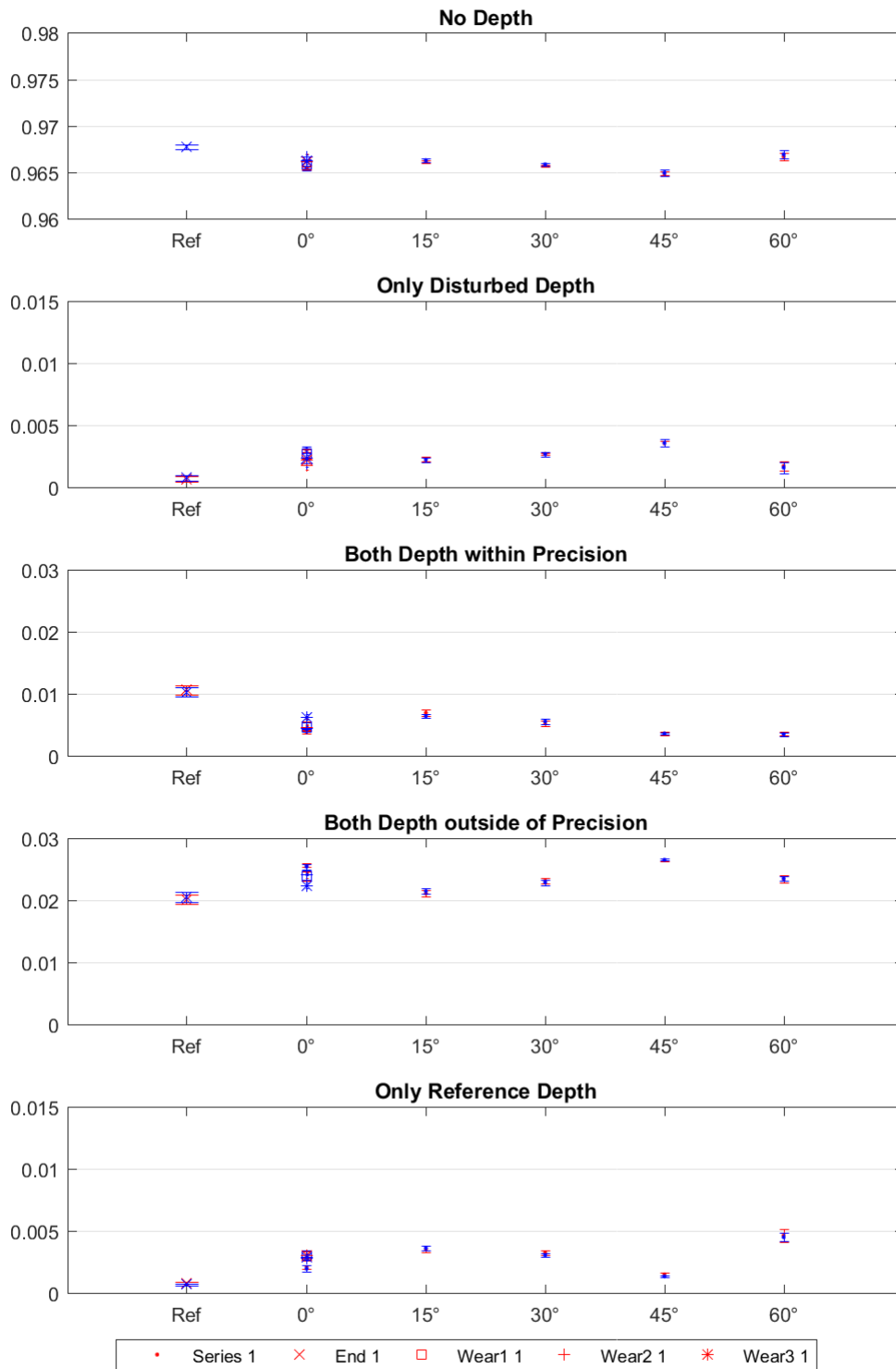


Fig. 6–2: Categorized depth densities for glass with fixed target distance. The red and blue points are from two consecutive image series.

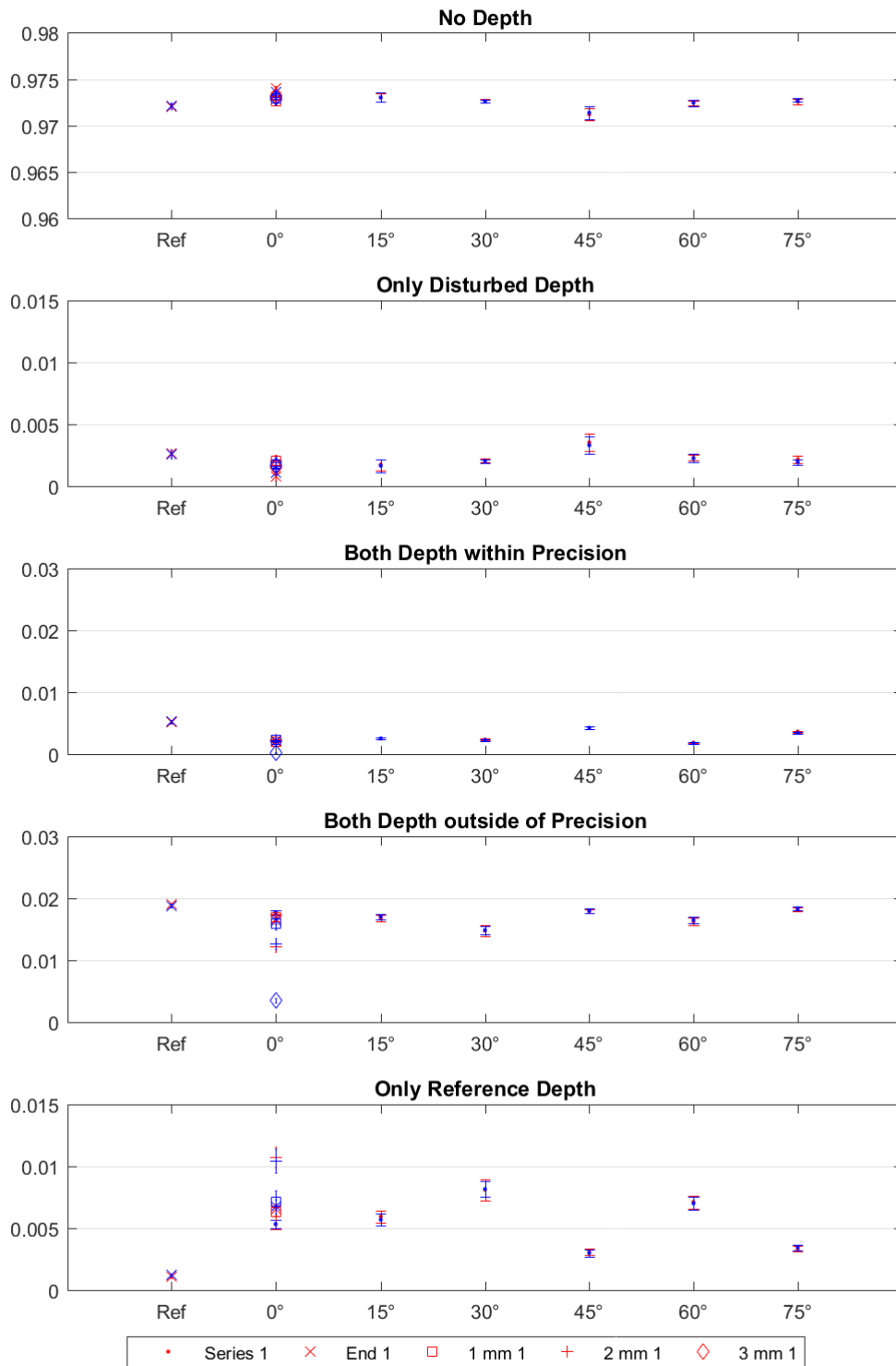


Fig. 6–3: Categorized depth densities for Makrolon® with fixed target distance. The red and blue points are from two consecutive image series.